

Submitted by  
**Julian Hofer, B.Sc.**

Submitted at  
**Institute of Semiconductor and Solid State Physics**

Supervisor  
**Prof. Dr. Armando Rastelli**

Co-Supervisor  
**DI Christian Schimpf**

month year

# **Advanced excitation and spectroscopy schemes with quantum dots**



Master Thesis  
to obtain the academic degree of  
**Diplom-Ingenieur**  
in the Master's Program  
**Technische Physik**



---

## **Eidesstattliche Erklärung**

Ich erkläre an Eides statt, dass ich die vorliegende Masterarbeit selbstständig und ohne fremde Hilfe verfasst, andere als die angegebenen Quellen und Hilfsmittel nicht benutzt bzw. die wörtlich oder sinngemäß entnommenen Stellen als solche kenntlich gemacht habe. Die vorliegende Masterarbeit ist mit dem elektronisch übermittelten Textdokument identisch.

---

Datum

---

Unterschrift



# Acknowledgement

First I would like to thank the head of our group Armando Rastelli for offering me this position and for making sure to always have an open ear, no matter how busy he was at the moment. I would also like to thank Christian Schimpf for taking the role as my unofficial supervisor. I can not think of anyone who would have fulfilled it better than him. Thanks belongs to most of my group members but I want to especially highlight Marcus Reindl and Daniel Huber who granted me the biggest support. Further, I would like to thank Susanne Schwind for solving every administrative issue that came along my way.

Last but not least, I would like to thank my parents for supporting every goal I have ever pursued in my life and of course Sabrina for more reasons than I could ever possibly list.<sup>1</sup>

---

<sup>1</sup>This document is set in Palatino, compiled with pdfL<sup>A</sup>T<sub>E</sub>X2e and Biber. The L<sup>A</sup>T<sub>E</sub>X template from Karl Voit is based on KOMA script and can be found online: <https://github.com/novoid/LaTeX-KOMA-template>



# Zusammenfassung

Geräte, die auf Quantentechnologie basieren, sind prädestiniert, Teil unseres täglichen Lebens zu werden. Halbleiterquantenpunkte mit ihren diskreten elektronischen Zuständen sind vielversprechende Kandidaten für dieses Gebiet und ideal für die Erforschung der Quantenoptik. Aus diesem Grund werden in dieser Arbeit zunächst Herstellungsverfahren und optische Eigenschaften von GaAs-Quantenpunkten vorgestellt.

Die weitere Diskussion ist in zwei Kapitel unterteilt, deren gemeinsamer Nenner GaAs-Quantenpunkte sind. Das erste befasst sich mit der resonanten Zwei-Photonen-Anregung mittels "adiabatic rapid passage". Bei diesem Verfahren werden gechirpte Laserpulse verwendet, deren Charakterisierung, Simulation und Messung den größten Teil dieses Kapitels ausfüllen. Der zweite Teil behandelt die spektrale Auflösung der Quantenpunktemission mittels eines Scanning Fabry-Pérot-Interferometers. Hier wird der Leser zunächst durch den Aufbau der mathematischen Beschreibung der Fabry-Pérot-Modi geführt. Anschließend werden Simulationen vorgestellt, mit deren Hilfe die Komponenten des Interferometers dimensioniert werden. Schließlich wird die Feinstruktur des Biexcitons im Rahmen

Zusammenfassung eines Proof-of-Principle-Experiments aufgelöst.

nach Abstract  
anpassen



# Abstract

Devices based on quantum technology are promising candidates to become part of our everyday lives. Semiconductor quantum dots with their discrete electronic states are promising candidates for this field and are ideal for research in quantum optics. That is why this thesis starts by introducing fabrication methods and optical properties of droplet-etched GaAs quantum dots.

The further work is splitted in two chapters with GaAs quantum dots as their common denominator. The first one deals with resonant two-photon excitation via adiabatic rapid passage. In this procedure chirped laser pulses are used and their characterization, simulation and measurements will fill the majority of this chapter. The second one investigates the capabilities of resolving quantum dot emission with a scanning Fabry Pérot interferometer. Initially, the reader is guided through the build-up of the mathematical description of the Fabry Pérot modes. Afterwards, simulations will be presented which are used to size the interferometer components. Finally the fine-structure of the biexciton will be resolved in a proof-of-principle experiment.

The detailed outlook over the chapters should be part of the introduction, not of the abstract.

Rewrite the abstract to give a brief overlook over all the work you did.



# Contents

## Zusammenfassung

## Abstract

<b>1. Introduction</b>	<b>1</b>
<b>2. Droplet etched gallium arsenide quantum dots</b>	<b>3</b>
2.1. Fabrication and optical properties . . . . .	3
2.2. Fine structur splitting . . . . .	6
2.3. Zero-phonon line and phonon sideband . . . . .	8
2.4. Optical excitation of a quantum dot . . . . .	11
2.5. Single photon emission . . . . .	12
<b>3. Methods</b>	<b>15</b>
3.1. Optical setup . . . . .	15
3.2. Pulse shaper . . . . .	16
3.3. Micro photo-luminescence . . . . .	16
<b>4. Entangled photon generation using adiabatic rapid passage with frequency-chirped pulses</b>	<b>19</b>
4.1. Introduction and motivation . . . . .	19
4.2. Chirp . . . . .	19
4.3. Measuring the chirp with interferometric autocorrelation . . . . .	22
4.4. Deterministically adjusting the chirp with a pulse expander . . . . .	25
4.5. Adiabatic rapid passage . . . . .	26
4.6. Measurements and discussion . . . . .	28
<b>5. Building up a scanning Fabry-Pérot interferometer from scratch</b>	<b>31</b>
5.1. Introduction and motivation . . . . .	31

5.2.	Transverse modes of electromagnetic radiation . . . . .	31
5.2.1.	Gaussian beam . . . . .	31
5.2.2.	Higher Gauss modes . . . . .	34
5.3.	Fundamentals of Fabry-Pérot interferometers . . . . .	35
5.3.1.	Resonator losses . . . . .	35
5.3.2.	Resonance frequencies, free spectral range and spectral line shapes . . . . .	36
5.3.3.	Airy distribution of Fabry-Pérot interferometers . . . . .	37
5.3.4.	Airy linewidth and finesse . . . . .	38
5.3.5.	Mode matching and spatial filtering . . . . .	40
5.3.6.	Confocal setup . . . . .	43
5.4.	Simulation . . . . .	44
5.5.	Setup and measurement . . . . .	47
5.5.1.	Scanning mode with fast photodiodes . . . . .	49
5.5.2.	Scanning mode with CCD . . . . .	50
5.6.	Measurements and discussion . . . . .	51
<b>6.</b>	<b>Summary and outlook</b>	<b>55</b>
<b>A.</b>	<b>Acronyms</b>	<b>59</b>
<b>Bibliography</b>		<b>61</b>

# List of Figures

2.1.	Droplet etched GaAs quantum dots. . . . .	4
2.2.	Biexciton-exciton cascade in a QD. The $ XX\rangle$ state can decay via two paths under the emission of a right (left) polarized photon into one of two energetically degenerated $ X\rangle$ states. The $ X\rangle$ state then decays into the ground state $ G\rangle$ under the emission of a left (right) polarized photon. [15] . . . . .	5
2.3.	Fine structure splitting in a GaAs quantum dot. . . . .	7
2.4.	Absorption line shape of an electronic excitation. . . . .	8
2.5.	Zero-phonon line and phonon sideband. [25] . . . . .	9
2.6.	Optical pumping of a QD by (a) above-band excitation and (b) resonant excitation [15]	11
2.7.	Resonant two photon excitation [16] . . . . .	12
2.8.	Hanbury-Brown-Twiss HBT experiment [16] . . . . .	13
3.1.	Complete experimental setup . . . . .	15
3.2.	Laser beam of different spot sizes illuminating quantum dots [32]. . . . .	17
4.1.	A chirped sinusoidal wave which increases in frequency over time. . . . .	20
4.2.	Electric field $E$ of Gaussian laser pulse of pulse duration $\tau_0 = 0.5 \text{ ps}$ for chirp of (a) $\alpha = 0 \text{ ps}^2$ and (b) $\alpha = 0.5 \text{ ps}^2$ . . . . .	21
4.3.	Schematics of an interferometric autocorrelator . . . . .	22
4.4.	Intensity of IAC of a Gaussian laser pulse of pulse duration $\tau_0 = 0.5 \text{ ps}$ with applied MOSAIC filter for chirp of (a) $\alpha = 0 \text{ ps}^2$ and (b) $\alpha = 0.5 \text{ ps}^2$ . . . . .	22
4.5.	Intensity of IAC of a Gaussian laser pulse of pulse duration $\tau_0 = 0.5 \text{ ps}$ with applied MOSAIC filter for chirp of (a) $\alpha = 0 \text{ ps}^2$ and (b) $\alpha = 0.5 \text{ ps}^2$ . . . . .	23
4.6.	Intensity of IAC of a Gaussian laser pulse of pulse duration $\tau_0 = 0.5 \text{ ps}$ with applied MOSAIC filter for chirp of (a) $\alpha = 0 \text{ ps}^2$ and (b) $\alpha = 0.5 \text{ ps}^2$ . The orange dots are results of a numerical peak finder algorithm, executed in order to find local minima. . . . .	24

---

4.7.	Intensity of IAC of a Gaussian laser pulse of pulse duration $\tau_0 = 0.5 \text{ ps}$ with applied MOSAIC filter and fitted $\alpha$ -values. . . . .	25
4.8.	Scheme of a folded pulse expander as described by Martinez [38]. The light enters on the right side, passes the halfmirror, and enters the system of transmission grating, lens and mirrors. Afterwards it hits the halfmirror and exits on the left hand. . . . .	25
4.9.	Influence of group velocity dispersion for example inside a fiber on a Gaussian pulse [39]	26
4.10.	Final biexciton occupation after chirped Gaussian pulse of pulse duration $\tau_0 = 2 \text{ ps}$ . .	27
4.11.	Measured IAC of Ti:Sa Laser without (a) and with (b) pulse expander before the autocorrelator. . . . .	28
4.12.	Measured IAC of Ti:Sa Laser with applied MOSAIC filter without (a) and with (b) pulse expander before the autocorrelator. . . . .	29
5.1.	A Gaussian beam near its beam waist. . . . .	33
5.2.	Gaussian modes higher order of a simple Ti-sapphire laser . . . . .	35
5.3.	Fabry P��rot interferometer with electric field mirror reflectivities $r_1$ and $r_2$ . . . . .	37
5.4.	Airy distribution $A'_{trans}$ . . . . .	38
5.5.	Demonstration of the physical meaning of the Airy finesse $F_{Airy}$ . . . . .	39
5.6.	Incident monochromatic beam of light exciting transverse mode $m, n$ of a resonator [45]	40
5.7.	Mode matching of an Gaussian beam into a Fabry P��rot interferometer. . . . .	41
5.8.	Spatial filtering of Gauss modes. . . . .	43
5.9.	Simulated exciton emission of a GaAs quantum dot . . . . .	45
5.10.	Transmission of the FPI modes $A'_{trans}$ compared to the exciton emission $\Phi_{dot}(E)$ for (a) ZPL and (b) PSB. . . . .	45
5.11.	Transmissions of the FPI modes $A'_{trans}$ (blue) for different mirror distances $l - m \cdot \Delta l$ with $m \in \mathbb{N}$ compared to the exciton emission $\Phi_{dot}(E)$ (red). . . . .	46
5.12.	Output-photon-flux of the scanning FPI $\Phi_{FPI}(E)$ (blue) compared to the exciton emission $\Phi_{dot}(E)$ (red) for (a) ZPI and (b) PSB. . . . .	46
5.13.	In (a) the shifted output-photon-flux of the scanning FPI $\bar{\Phi}_{FPI}(E)$ (blue) compared to the exciton emission $\Phi_{dot}(E)$ (red) is displayed. In (b) the absolute difference between those two $ \bar{\Phi}_{FPI}(E) - \Phi_{dot}(E) $ (light blue) is additionally shown. . . . .	47
5.14.	Comparison between two setups where one uses bigger, planar mirrors and one uses smaller, planar-convex mirrors . . . . .	48
5.15.	Top view of FPI and casing. . . . .	49

## List of Figures

---

5.16. Live avalanche photodiode setup with using a function generator driving the piezo actuator of the FPI and the sync input of the correlation hardware. APDs are used because of their speed, allowing to live-adjusting the FPI-parameters. . . . .	49
5.17. Measurement of scanning FPI with APDs. The scanning frequency is 5 Hz and the range is 1 $\mu\text{m}$ . The measured finesse is $\approx 5$ and the free spectral range corresponds to 280 nm. . . . .	50
5.18. Scanning Fabry Pérot interferometer with CCD . . . . .	51
5.19. Aligning the Fabry Pérot interferometer . . . . .	51
5.20. Transmission measurement of FPI with ground mirror distance $l \approx 2 \text{ mm}$ and HeNe laser. (a) was aligned without spatial filtering with a pinhole and (b) involved a pinhole. . . . .	52
5.21. Polarization map of exciton of QD in sample AS208. . . . .	52
5.22. Finestructure measurement of biexcitation of QD in sample AS208 by passing through FPI and sweeping the mirror distance. Ground mirror distance was $l \approx 2 \text{ mm}$ . . . . .	53



## **Todo list**

Zusammenfassung nach Abstract anpassen . . . . .

The detailed outlook over the chapters should be part of the introduction, not of the abstract.

Rewrite the abstract to give a brief overlook over all the work you did. . . . .

What does this comparison tell us? Did it fit the calculation? Where are the side peaks we saw in the HeNe measurement? What about the stability? Are there calculations, expected temperature drifts, etc. Are there differences between the expected Finesse and the measured one, and why? Is this expected? . . . . .

53

Don't refer all the time to the main text. Imagine I'm a reader from a different field. I read the abstract, the introduction and the summary/outlook. Now I should know what you did and why and what are the future plans. At this point I have no idea what MOSAIC is, I have no idea what a pulse expander is, etc. unless you give me a hint in the summary. . .

55

# 1. Introduction

In the past century, technology was transformed by the first quantum revolution. Scientists and engineers all around the world utilized certain features of quantum mechanics such as energy quantization and wave-particle duality to create devices which are nowadays a fixed part of everyone's life [1]. These technologies, ranging from semiconductor devices to LEDs and lasers, became high-performance components which drive modern information processing and global communication networks. The second quantum revolution will make use of superposition and entanglement [2].

Entanglement is already the basis of many experiments in quantum computation and its distinct properties can be used for quantum cryptography protocols as well. [3]. It describes a physical phenomenon involving two or more particles which quantum states cannot be described independently from each other. Entanglement is especially useful when the entangled particles are photons, as these can be transported over long distances with optical fibres and are therefore ideal to build up quantum networks [4]. Quantum key distribution QKD under the E91 protocol can use the quantum network to exchange entangled photons and then generate a shared encryption key. Since the photons are entangled, the key can be generated in a way which prevents an eavesdropper to obtain the same key without the parties wishing to communicate to notice. The key is then used to encrypt the data by one party, the encrypted data is transmitted via classical channels and afterwards decrypted with the very same key by the other party. The E91 protocol with its use of entanglement has the advantage that it guarantees to detect eavesdropping even with lossy channels, which is a guarantee other implementations of QKD cannot necessarily fulfil [5].

However, in order to use entangled photons for QKD several problems have to be solved first. Fibre channels suffer from de-coherence and optical losses, degrading the quantum information to a point where they are unusable for quantum protocols and therefore limiting the maximal communication distance. Usually classical amplifiers would be used in order to counteract transmission losses, however this does not work with quantum states. In order to solve this problems, multiple teams are in the process of developing quantum repeaters [6][7][8]. Quantum repeaters use quantum teleportation

## 1. Introduction

---

as it performs a Bell state measurement with the photon to transmit and a photon entangled to a photon at the next repeater station. The bell state in order to transmit a quantum state to another location by performing a Bell state measurement (BSM) [9]. The BSM teleports the quantum state to the photon at the next repeater station, while destroying the quantum state of the two measured photons in accordance with the no cloning theorem [10]. Therefore, the transmission distance can be broken up into segments where the losses are acceptable.

Additionally, the E91 protocol requires deterministic sources of single entangled photons. Two prominent sources are parametric down conversion crystals [11] and single atoms [12]. Sources based on parametric down conversion are currently the brightest ones, however their emission is probabilistic, which means that the number of entangled photon pairs emitted per excitation pulse is statistically distributed. This can be overcome by filtering which has the disadvantage of reducing the throughput. Single atoms offer sharp electronic transitions, are free from charge fluctuations and are energetically isolated. Nowadays advanced techniques [13] are used in order to operate with single-atom-based sources, but their dynamics are still relatively low, leading to slow operation rates.

Quantum dots provide an alternative source of single entangled photons. Quantum dots are deterministic, emitting maximal one photon pair per excitation and are scalable to nanosized dimensions. With this motivation in mind, droplet-etched GaAs quantum dots as potential sources are investigated in chapter 2, as they are quasi strain-free, of high symmetry and exhibit low values of fine structure splitting (FSS). Entanglement fidelity is limited by re-excitation of photons at the exciton level to the biexciton level before they can decay to the ground state, but this effect can be avoided by resonant two-photon excitation. Resonant two-photon excitation usually requires precise control of the intensity of the exciting field in order to inverse the quantum dot from the ground state to the biexciton state [14]. Adiabatic rapid passage with frequency-chirped pulses does not suffer from this requirement, which motivates its discussion in chapter 4.

When it then comes to characterizing quantum dot (QD) emission, more obstacles arise as fine features of the emission spectrum are not resolvable with a CCD-based spectrometer alone. A Fabry-Pérot interferometer can be used to resolve QD emission while still using the same spectrometer. It transmits signals of certain frequencies and these frequencies can be adjusted in order to scan through the ranges of interest. QD emission can be sent through the scanning interferometer and its output could then be recorded with the CCD allowing to reassemble the complete spectrum. Chapter 5 describes the efforts to build up a scanning Fabry-Pérot interferometer to do exactly that.

## 2. Droplet etched gallium arsenide quantum dots

### 2.1. Fabrication and optical properties

Quantum dots (QD) are nanostructures which confine the motion of electrons and holes in all three spatial dimensions. Confinement results in discrete energy levels, which is why QDs are sometimes referred to as *artificial atoms*. The discussion in this section is based on the PhD thesis of Huber [15] and on the master's thesis of Schimpf [16].

Gallium arsenide QDs investigated within this master's thesis are grown by molecular beam epitaxy (MBE) with the self-assembled nanodrill technology described in the work of Wang et al. [17]. As displayed in figure 2.1a the Al forms droplets on  $\text{Al}_{0.4}\text{Ga}_{0.6}\text{As}$  after evaporation. The Al reacts with  $\text{Al}_{0.4}\text{Ga}_{0.6}\text{As}$ , etching nanoholes into the surface. Under ideal conditions, these nanoholes are highly symmetric resulting into QDs with high in-plane symmetry as can be seen in figure 2.1b. The next step is the annealing process in which GaAs is deposited to fill the nanoholes. The QD is finalized by capping the layer with  $\text{Al}_{0.4}\text{Ga}_{0.6}\text{As}$  acting as top barrier.

Compared to the band gap of the host material  $\text{Al}_{0.4}\text{Ga}_{0.6}\text{As}$  of 1.92 eV at room temperature, the core of the QD, GaAs has a band gap of only 1.42 eV at room temperature. The energy difference between the bandgaps and the discrete energy levels forming in the QD are responsible for the 3D confinement and the type-I band alignment depicted in figure 2.1c. Inside of the QD, optical transitions are possible. Transitions between the first energy level in the conduction band (CB) and the valence band (VB), often called the s-shell, are here of special interest. The carriers involved are the electrons ( $e^-$ ) and the holes ( $h^+$ ) left behind. These are fermions and therefore only up to two of them can, in accordance with Pauli's exclusion principle, occupy a single energy state. Electrons and holes are strongly localized inside the QD by the confinement potential and influence each other by Coulomb attraction and

## 2. Droplet etched gallium arsenide quantum dots

exchange interaction [18]. This leads to multi-particle complexes with the most fundamental being the exciton ( $X$ ), a quasi-particle consisting of an electron and a hole, bound by Coulomb interaction. Fully occupied s-shells form the biexciton ( $XX$ ), consisting of two electrons and two holes of opposite spins.

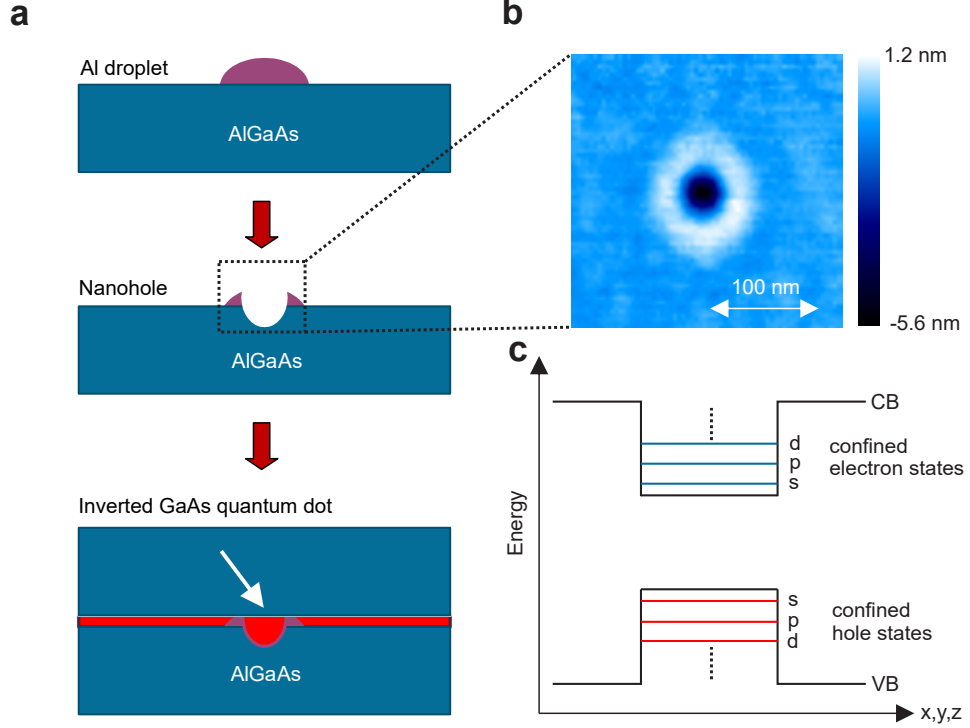


Figure 2.1.: (a) The growth process of a GaAs quantum dot by MBE.  
 (b) Atomic force microscopy (AFM) image of the nanohole before it is filled with GaAs.  
 (c) Conduction band (CB) and valence band (VB) of an optically active QD. [15]

In a QD, polarization-entangled photon pairs can be generated via a biexciton-exciton decay cascade [19], illustrated in figure 2.2. The  $|XX\rangle$  state forms a full shell, which means that the total angular momentum projection along the quantization axis of the  $XX$  complex sums up to  $M = 0$ . The QD is radially symmetric, therefore  $M$  is preserved and  $|M\rangle$  are eigenstates of the system. After exciting the QD into the  $|XX\rangle$  state (e.g. by optical pumping) it decays by spontaneous recombination of an electron-hole-pair accompanied by the emission of a single photon into the  $|X\rangle$  state.

The two dipole-allowed radiative transitions lead to only two possible angular momentum states of the exciton:

- $| -1 \rangle$  under emission of a right-circularly-polarized photon  $| R_{XX} \rangle$
- $| +1 \rangle$  under emission of a left-circularly-polarized photon  $| L_{XX} \rangle$

$| -1 \rangle$  and  $| +1 \rangle$  are degenerated in energy and decay into the groundstate  $| G \rangle$  under emission of  $| L_X \rangle$  and  $| R_X \rangle$ , respectively. The resulting two-photon state is then described by

$$| \psi^+ \rangle = \frac{1}{\sqrt{2}} (| L_{XX} \rangle | R_X \rangle + | R_{XX} \rangle | L_X \rangle) \quad (2.1)$$

which is one of the four Bell states, representing the maximal entangled two-particle states.

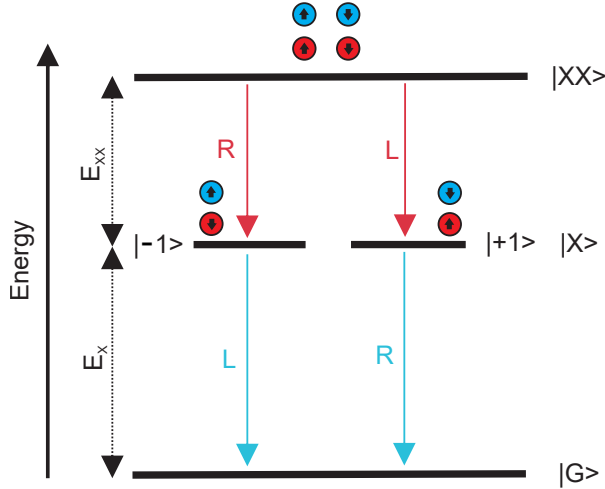


Figure 2.2.: Biexciton-exciton cascade in a QD. The  $| XX \rangle$  state can decay via two paths under the emission of a right (left) polarized photon into one of two energetically degenerated  $| X \rangle$  states. The  $| X \rangle$  state then decays into the ground state  $| G \rangle$  under the emission of a left (right) polarized photon. [15]

In order to calculate the life time of the  $X$  and  $XX$  states and the respective spectral description of the emission the radiative transition rate  $\Gamma$  between quantum mechanical states has to be derived.  $\Gamma$  describes the transition probability per unit time from an initial state  $| i \rangle$  to a final state  $| f \rangle$  and can be calculated by Fermi's golden rule if the transition occurs because of a weak perturbation. In the dipole approximation it depends on

$$\Gamma \propto |\langle f | \mathbf{e} \cdot \hat{\mathbf{p}} | i \rangle|^2 \delta(E_i - E_f - E_P) \quad (2.2)$$

with  $\mathbf{e}$  as the unit polarisation vector of the emission,  $\hat{\mathbf{p}}$  as the momentum operator of the electron and  $E_f$ ,  $E_i$  and  $E_P$  as the energies of the final state, of the initial state and of the emitted photon

## 2. Droplet etched gallium arsenide quantum dots

---

respectively. The rate equation for the population of the initial state can then be described by

$$\frac{dN_i(t)}{dt} = -\Gamma N_i(t) \quad (2.3)$$

which results into a potential decays as solution

$$N_i(t) = N_i(0)e^{-t/\tau} \quad (2.4)$$

where the lifetime of the initial state is defined as  $\tau = 1/\Gamma$ .

This can be applied for the X and XX states with decay constants  $\tau_\nu$  and intensity for the emitted light  $I_\nu(t)$  where  $\nu \in \{X, XX\}$ . The Fourier transformation of the electric field yields a Cauchy distribution

$$I_\nu(\omega) = \frac{1}{2\pi\tau_\nu} \frac{1}{(\omega - \omega_\nu)^2 + \left(\frac{1}{2\tau_\nu}\right)^2} \quad (2.5)$$

with  $\omega_\nu = e_\nu/\hbar$  as its center frequency.

## 2.2. Fine structur splitting

Fine structure splitting (FSS) in a QD describes the energy splitting between the two possible bright  $|X\rangle$  states. In GaAs it originates from the exchange interaction between electrons and holes. [20]. The electron-hole exchange Hamiltonian is described by

$$\mathcal{H}_{ex} = - \sum_{i=x,y,z} a_i J_{h,i} S_{e_i} + b_i J_{h,i}^3 S_{e_i} \quad (2.6)$$

with  $a_i$  and  $b_i$  as the spin-coupling constants,  $J_{h,i}$  as the holes' and  $S_{e_i}$  the electrons' total angular momentum. The z-direction is assigned as the crystal growth direction and the bright X states are defined by the projections of  $J_{h,i}$  and  $S_{e_i}$  to the z-axis, so that  $|+1\rangle = |+\frac{3}{2}, -\frac{1}{2}\rangle$  and  $| -1\rangle = |-\frac{3}{2}, +\frac{1}{2}\rangle$ . The Hamiltonian of equation (2.6) can then be described in the bases  $\{|+1\rangle, |-1\rangle\}$

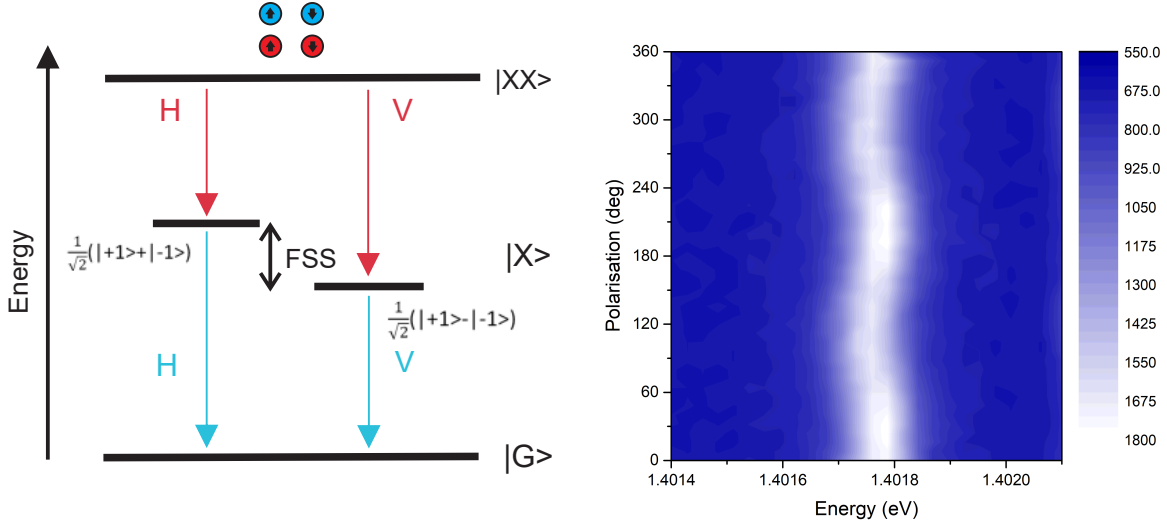
$$\mathcal{H}_{ex} = \begin{pmatrix} \langle +1|\mathcal{H}_{|S}|+1\rangle & \langle +1|\mathcal{H}_{|S}|-1\rangle \\ \langle -1|\mathcal{H}_{|S}|+1\rangle & \langle -1|\mathcal{H}_{|S}|-1\rangle \end{pmatrix} = \begin{pmatrix} \Delta_0 & \Delta_1 \\ \Delta_1 & \Delta_0 \end{pmatrix} \quad (2.7)$$

with  $\Delta_0 = \frac{3}{4}(a_z + \frac{9}{4}b_z)$  and  $\Delta_1 = -\frac{3}{8}(b_x - b_y)$ .

In the ideal case the QD is perfectly symmetric along the z-axis,  $b_x = b_y$ ,  $\Delta_1$  vanishes and  $|+1\rangle$  and  $| -1\rangle$  are degenerate eigenstates. If that is not the case, the angular momentum  $M$  along the z-direction is not preserved and  $|+1\rangle$  and  $| -1\rangle$  are no eigenstates of  $\mathcal{H}_{ex}$ . The new basis can be found

## 2.2. Fine structure splitting

by diagonalising  $\mathcal{H}_{ex}$  and are described by  $\frac{1}{\sqrt{2}}(|+1\rangle + |-1\rangle)$  and  $\frac{1}{\sqrt{2}}(|+1\rangle - |-1\rangle)$ . In figure 2.3a the  $|XX\rangle$  decay path with splitted  $|X\rangle$  eigenstates is shown.  $|XX\rangle$  exhibit no splitting as the angular momentum of the electrons and holes add to zero and therefore no exchange interaction occurs. In figure 2.3b photo-luminescence spectra recorded with a linear polariser are shown.



(a) XX decay cascade without X degeneracy because of fine structure splitting. [15]

(b) Photoluminescence spectra of X emission of a GaAs Qd plotted for different polarizer angles. In the image the effect of the linear polarization of the fine structure components is visible. [16]

Figure 2.3.: Fine structure splitting in a GaAs quantum dot.

### 2.3. Zero-phonon line and phonon sideband

The excitonic emission of GaAs QDs exhibits non-Lorentzian asymmetric broadening. These side bands can be traced back to a coupling to acoustic phonons [21][22]. The discussion of phonon side bands (PSBs) is based on the works of Friedrich and Haarer [23] and Peter et al. [21].

Figure 2.4 displays a schematic representation of the zero phonon line (ZPL) and PSB absorption spectrum. The intensity distribution between the two components depends strongly on temperature.

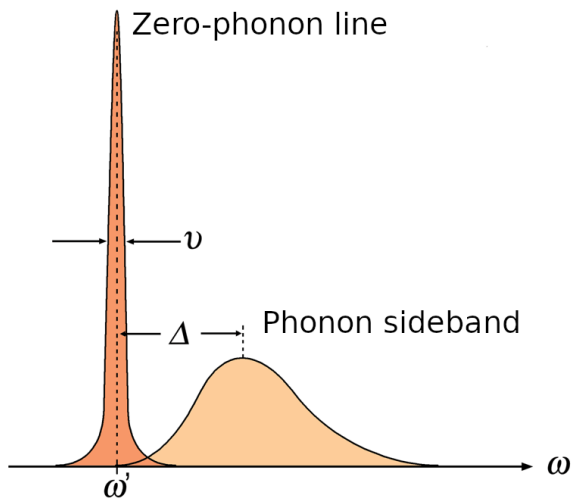
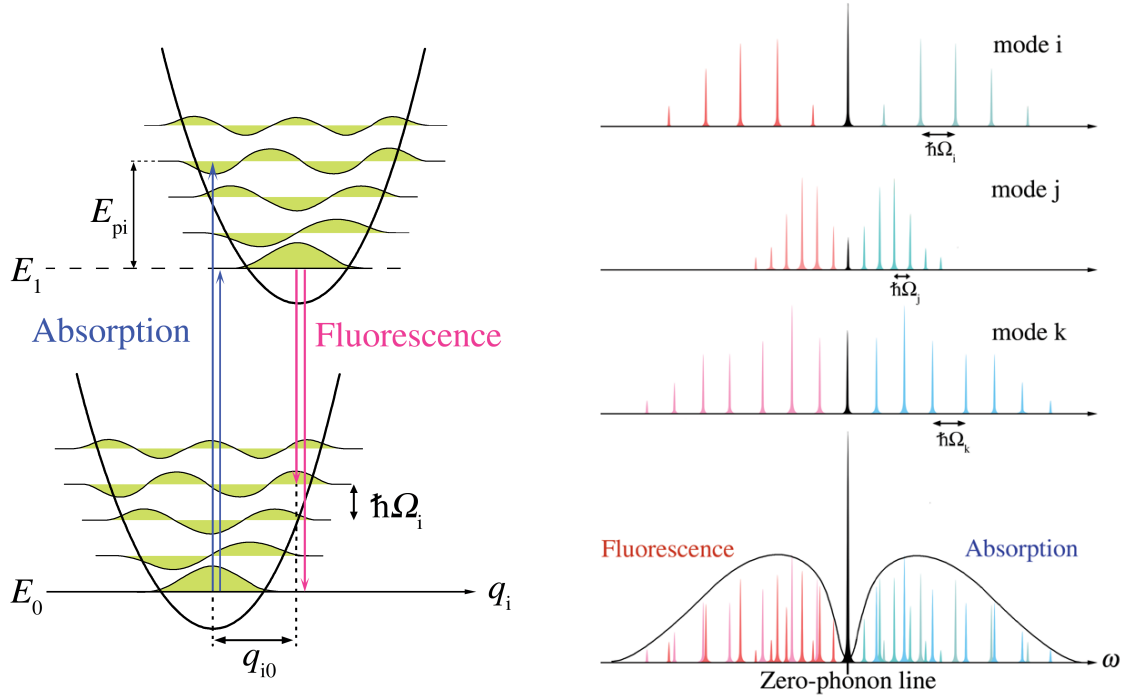


Figure 2.4.: Absorption line shape of an electronic excitation. The emission shape can be determined by mirroring the absorption shape at  $\omega'$ .

To determine the frequency gap  $\Delta$  in figure 2.4, the Franc-Condon principles (FCP) [24] are used. The FCP state that electronic transition between ground and excited state is much faster than the motion in the lattice as the photons carry nearly no momentum. Hence, there is no motion along the configurational coordinates  $q_i$  during the energy transitions as depicted in figure 2.5a. The transitions can be displayed as vertical arrows with the shorter arrow describing the ZPL and the longer one describing the PSB. According to the FCP, the more the wave functions of two vibrational energy levels overlap, the likelier is the electronic transition between these two. In the case of figure 2.5a this occurs when the photon energy equals to the energy difference  $E_1 - E_0$  plus three quanta of vibrational energy  $E_{pi} = \hbar\Omega_i$ . The emission follows the same principle.



(a) Energy spectrum of a two-level electronic system with phonon coupling. The arrows describe emission/absorption with and without phonons respectively.

(b) Three lattice normal modes ( $i, j, k$ ) and the resulting emission/absorption spectrum.

Figure 2.5.: Zero-phonon line and phonon sideband. [25]

Figure 2.5a and 2.5b implicitly assume approximations in addition to the FCP. The lattice vibrational mode has to be well described by a quantum harmonic oscillator. Additionally, it is assumed that only the lowest lattice vibration is excited and that the harmonic oscillator potentials are equal in both states. These preconditions are visible in the parabolic shaped potential wells and equally spaced phonon energy levels in figure 2.5a.

The reason why the ZPL is stronger than the PSB can be found by examining the superposition of the lattice modes. Each lattice mode  $m$  leads to a different energy difference  $\hbar\Omega_m$  between phonons. That is why the transitions with phonons result in a energy distribution and the zero-phonon transition add up at the electronic origin  $E_1 - E_0$  as can be seen in figure 2.5bb.

## 2. Droplet etched gallium arsenide quantum dots

---

The theoretical limit of the spectral range of the zero-phonon line for a GaAs quantum dot can be calculated with the time-energy uncertainty relation

$$\Delta E \cdot \Delta t = \frac{h}{2\pi} \quad (2.8)$$

This gives for typical lifetime of a GaAs quantum dot of  $\Delta t = 250 \text{ ps}$

$$\Delta E = 2.64 \mu\text{eV}. \quad (2.9)$$

The frequency uncertainty can be obtained through

$$\Delta\nu = \frac{\Delta E}{h}. \quad (2.10)$$

The wavelength  $\lambda$  relates to  $\nu$  with the Planck-Einstein relation

$$\lambda(\nu) = \frac{c}{\nu} \quad (2.11)$$

and the wavelength uncertainty  $\Delta\lambda$  can be approximated with a Taylor series around  $\nu_0$

$$\Delta\lambda = -\lambda'(\nu_0) \cdot \Delta\nu. \quad (2.12)$$

With equation (2.10) and the center wavelength of the zero-phonon line  $\lambda_0$  in table 2.1 this gives

$$\Delta\lambda = \frac{c}{\nu_0^2} \cdot \Delta\nu = \frac{\lambda_0^2}{c} \cdot \Delta\nu \quad (2.13)$$

$$\approx 1.0 \text{ pm} \quad (2.14)$$

Together with data from Schöll et al. [26] and empirical values measured by our group, this leads to the parameters listed in table 2.1.

Table 2.1.: Parameters of GaAs quantum dots used in the laboratory of semiconductor physics department in Linz. Zero-phonon line calculates from the theoretical limit according to the life time of the excitonic state (as can be seen in equation (2.14)) up to broader lines which are still valued enough to be measured. The phonon sideband resembles data taken from Schöll et al. [26].

Quantum dot emission	Center wavelength $\lambda_0$	Spectral range $\Delta\lambda$	Waveform
Zero-phonon line	(700 to 800) nm	(1.0 to 1.4) pm	Cauchy
Phonon sideband	~0.25 nm higher than zero-phonon line	500 pm	Gauss

## 2.4. Optical excitation of a quantum dot

In this section, the different ways of optically exciting QDs are discussed. It is based on the PhD thesis of Huber [15] and the master's thesis of Schimpf [16]. The excited states of a QD can be populated in various ways. A common way is above-band excitation, depicted in figure 2.6a. Electrons are optically excited by a laser with energies above the band gap of the QDs host material  $\text{Al}_{0.4}\text{Ga}_{0.6}\text{As}$  with  $E_L = 1.92 \text{ eV}$  at room temperature. Subsequently, electrons and holes are captured by the QDs and relax via phonon-scattering to the lowest energy level, the s-shell. However, because of pronounced recapture processes [27] and spin scattering processes [28], above-band excitation is not favourable for entangled photon generation. Additionally, indistinguishability of the emitted photons is reduced because of fluctuating electric fields. Resonant excitation of electron-hole pairs provides an alternative which is less affected by fluctuating electric fields. As shown in figure 2.6b this technique creates electron-hole-pairs directly in the s-shell.

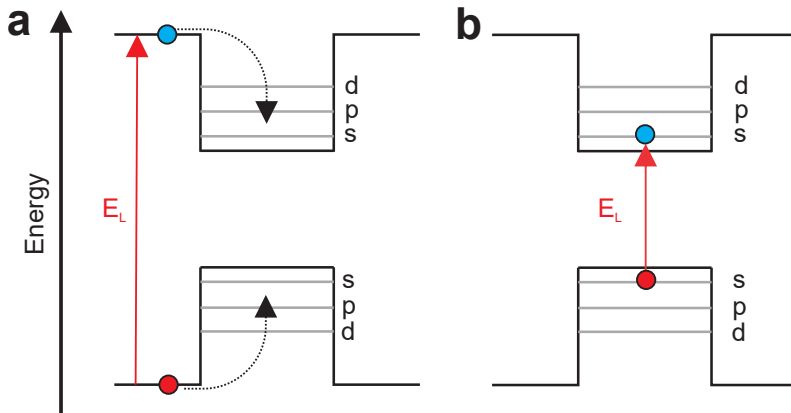


Figure 2.6.: Optical pumping of a QD by (a) above-band excitation and (b) resonant excitation [15]

Resonant excitation can be used in order to populate the  $|XX\rangle$  state with near unity population probability [29]. Due to dipole-selection rules, this requires a two-photon-absorption process. Hereby, the energy of a femtosecond-pulse laser  $E_p$  is tuned to exactly the half of the  $XX$  energy with respect to the ground energy, as sketched in figure 2.7a. Because of Coulomb interaction, two times the  $X$  energy with respect to the ground energy  $2 \cdot E_X$  is not equal to  $E_{XX}$  but differs by the binding energy  $E_B$ . The laser is therefore tuned to

$$E_p = E_X - E_B/2 \quad (2.15)$$

with empirically  $E_B \approx 3.78 \text{ meV}$  for GaAs QDs. Resonant two-photon absorption is a third-order

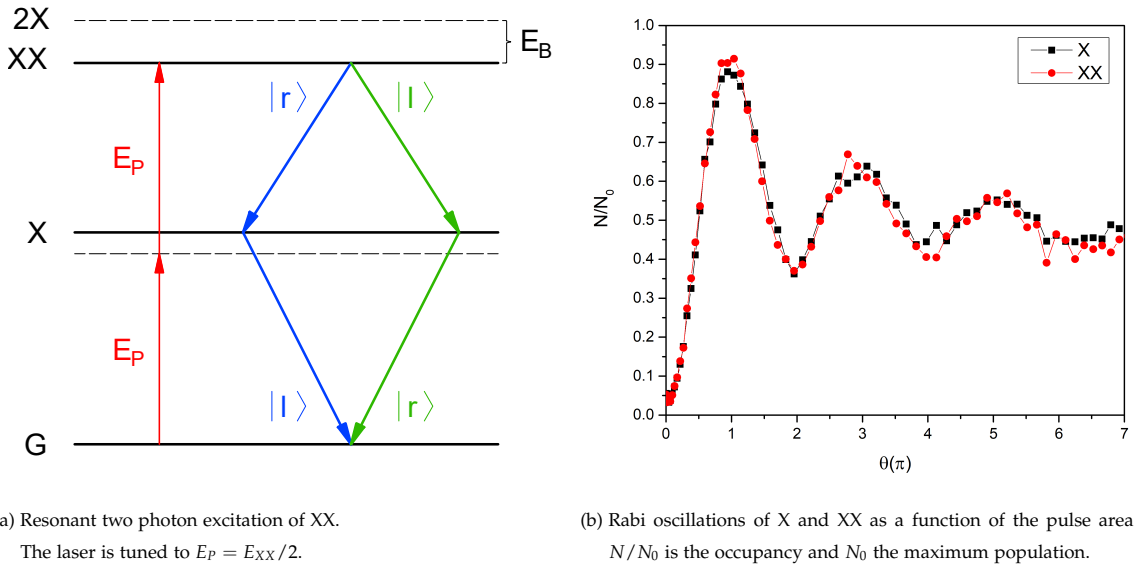
## 2. Droplet etched gallium arsenide quantum dots

non-linear effect which involves two photons and electrons at once. It depends on the third-order-susceptibility  $\chi^{(3)}$  of GaAs and therefore requires relatively high laser power.

As this two-level system is driven in resonance its population exhibits Rabi oscillations. The final population of the XX can be described by

$$N_{XX} = \sin^2\left(\frac{\theta}{2}\right) \quad (2.16)$$

with  $\theta$  as the pulse area in relation to the Rabi oscillations. It has to be noted that  $\theta$  is not the area of the excitation pulse, but depends on it in a non-trivial way [30]. Measured Rabi oscillations of X and XX are shown in figure 2.7b [29]. Theoretically, the curve should oscillate between occupancies  $N/N_0$ , with  $N_0$  as the maximum population, of 0 and 1. However, as a consequence of phonon damping the occupancy converges to a purely probabilistic value of 0.5 [31].



(a) Resonant two photon excitation of XX.

The laser is tuned to  $E_P = E_{XX}/2$ .

(b) Rabi oscillations of X and XX as a function of the pulse area  $\theta$ .

$N/N_0$  is the occupancy and  $N_0$  the maximum population.

Figure 2.7.: Resonant two photon excitation [16]

## 2.5. Single photon emission

The XX-X cascade shown in figure 2.7a results in a single photon pair per emission cycle. Single photons are necessary for quantum cryptography and quantum optics in general which motivates the following discussion of this topic based on the thesis of Huber [15]. The single photon purity of the  $|XX\rangle$  to  $|X\rangle$  and the  $|X\rangle$  to  $|G\rangle$  decay emissions, respectively, can be determined by performing a

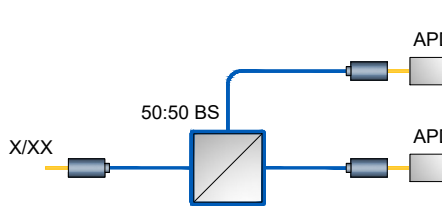
Hanbury-Brown-Twiss (HBT) experiment. An example of an HBT setup is shown in figure 2.8a and consists of two avalanche photodiodes (APDs) used as single photon detectors and a beam splitter. The measurements at the two detectors can be used in order to calculate the second-order correlation function

$$g^{(2)} = \frac{\langle n_1(t)n_2(t + \tau) \rangle}{\langle n_1(t) \rangle \langle n_2(t + \tau) \rangle} \quad (2.17)$$

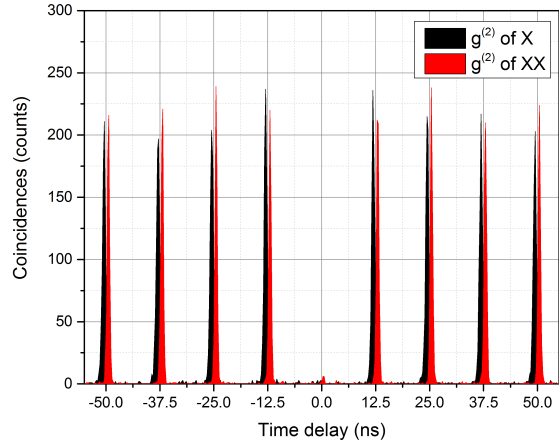
where  $n_i(t)$  is the number of counts registered on APD  $i$  at time  $t$  and  $\tau$  is the time delay. When a single photon enters the input of the beam splitter (BS) it can only be measured at one output, but never at both simultaneously. Assuming a perfect single photon emitter, a coincidence measurement between APD 1 and APD 2 will result in  $g^{(2)}(\tau = 0) = 0$ . Subsequently, side peaks are expected at  $\tau_s = z/R$  with  $R$  as the repetition rate of the laser and  $z \in \mathbb{Z} \setminus \{0\}$ . The single photon purity can then be defined as

$$\kappa(b) = \frac{A_0(b)}{A_s(b)} \quad (2.18)$$

with  $A_0$  as the area under  $g^{(2)}(\tau)$  around  $\tau = 0$  and  $A_s$  as the average area under the side peaks at  $\tau_s$ . The time bin  $b$  has to be chosen so that it includes a full side peak. If  $b$  would be chosen too small it would falsely increase  $\kappa$ , if chosen too high it includes unnecessary much noise.



(a) Setup to measure the Hanbury-Brown-Twiss effect. Single photons can be measured only at one APDs, but not at both at the same time.



(b) Second-order auto-correlation function  $g^{(2)}$  of X and XX. The low height of the peak at zero time delay compared to the height of the side peaks suggest the suitability of the quantum do as a single photon emitter.

Figure 2.8.: Hanbury-Brown-Twiss HBT experiment [16]



# 3. Methods

## 3.1. Optical setup

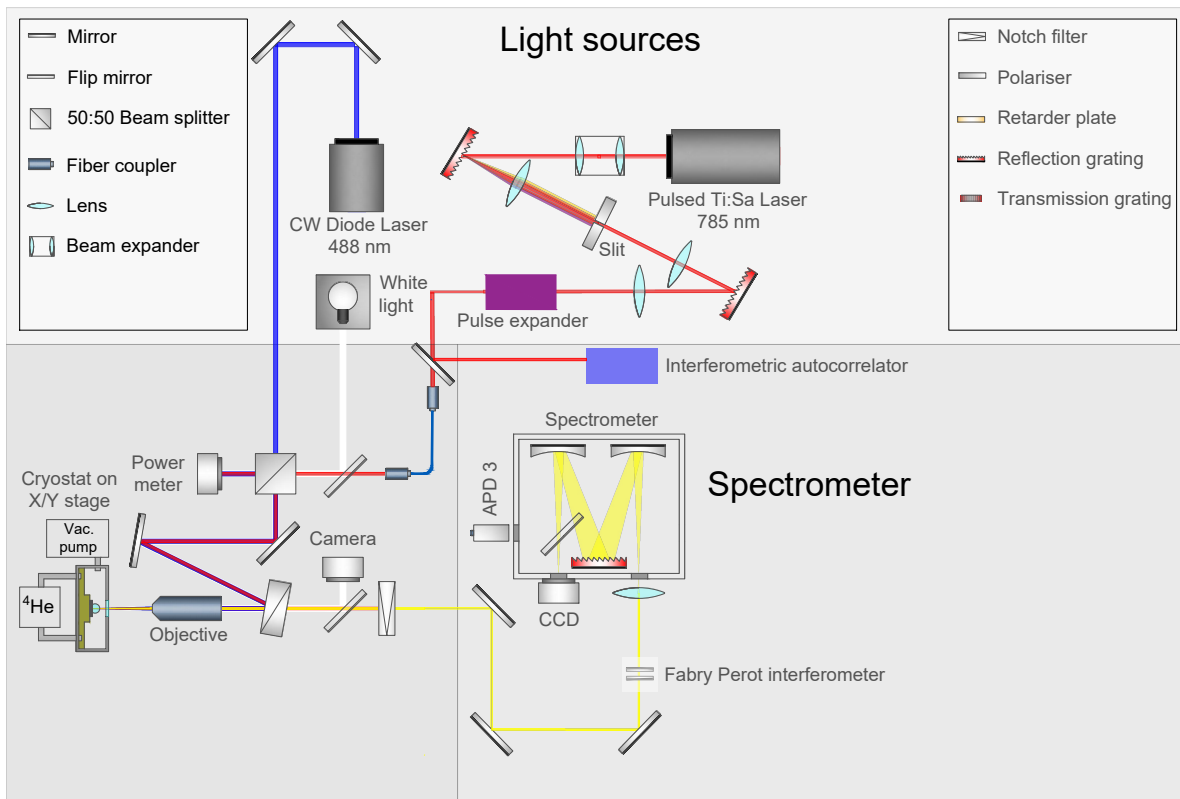


Figure 3.1.: Complete experimental setup, which was used in order to quantify the chirp of the Ti:Sa Laser and resolve spectral emission of a quantum dot [16].

The setup used for the measurements described in following chapters is sketched in figure 3.1. It involves a pulsed Ti:Sa laser which is sent through a pulse shaper and its chirp can be modified with

### 3. Methods

---

the pulse expander and measured with the interferometric autocorrelator as will be discussed in chapter 4. The CW diode laser is used in order to find a suitable QD and the white light enhances the brightness of some QDs. The spectrometer is then used to measure QD emission either with the CCD or the APD.

## 3.2. Pulse shaper

In order to resonantly excite the  $|XX\rangle$  state a pulsed Ti:Sa laser with a full width at half maximum (FWHM) pulse duration of  $\tau_P \approx 100$  fs is used. Under the assumption that the laser pulse is of Gaussian shape and that it is chirp-free (more on that in chapter 4), the spectral bandwidth  $\Delta\nu$  can be described by

$$\Delta\nu\tau_P \approx 0.44. \quad (3.1)$$

This corresponds to a spectral range of  $\Delta E = h\Delta\nu = 18.2$  meV. As can be seen in equation (2.15), the spectral range should be smaller than  $E_B/2 \approx 1.89$  meV, which is not fulfilled with the laser beam alone.

The pulse shaper sketched in the upper part of figure 3.1 is used in order to tune  $\Delta E$  and additionally the centre emission energy to our requirements. The laser beam is sent through a Keplerian telescope in order to expand its beam diameter from 3.4 mm to 6 mm. It gets dispersed by a diffraction grating and focused by a lens so that the spectral components are ordered along a plane where the slit is placed. The centre energy can be adjusted with the slit position and the spectral range with the slit width. The setup is mirrored with an additional lens and diffraction grating, which transform the laser beam again into real space.

## 3.3. Micro photo-luminescence

The following chapters will investigate the optical properties of QD. In order to achieve that, it is necessary to excite and collect light of only a single one. This is achieved by micro photo-luminescence (MPL), which involves (i) reducing the diameter of the excitation laser beam and (ii) using samples with a low QD density [32]. (i) can be improved by using an objective, where its minimal achievable spot size  $d$  is described by

$$d = \frac{\lambda}{2 \cdot NA} \quad (3.2)$$

with  $NA$  as the numerical aperture. As the wavelength of the laser  $\lambda$  is adjusted according parameter of the QD,  $NA$  is the adjustable factor. In our laboratory, an objective of  $NA = 0.62$  is used, allowing laser spot sizes in the order of the excitation wavelength. A QD density of  $\approx 1/\lambda^2$  is therefore necessary in order to examine single QD emission.

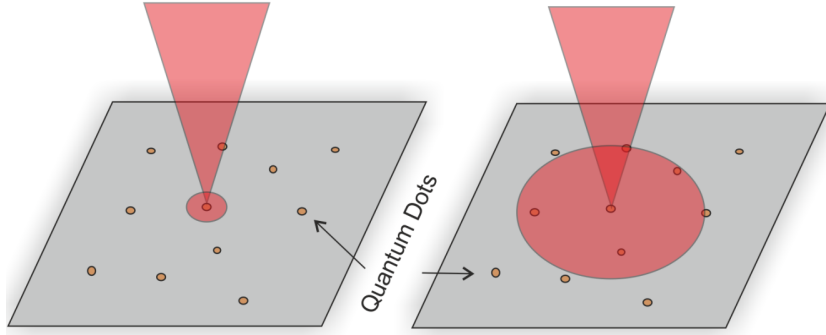


Figure 3.2.: Laser beam of different spot sizes illuminating quantum dots [32].

The sample containing the QDs is mounted inside the cryostat, which is cooled down to 4 K. This is necessary as the influence of dephasing processes increases with higher temperature due to carrier-phonon interaction. The laser beam is then focused on the sample by the objective and the QD emission is then collected by the very same objective and passed through a beam splitter.



## **4. Entangled photon generation using adiabatic rapid passage with frequency-chirped pulses**

### **4.1. Introduction and motivation**

In order to efficiently use the biexciton decay cascade, the biexciton state has to be prepared beforehand in a robust way. This chapter deals with the efficient inversion of the QD from the ground state to the biexciton level via adiabatic rapid passage (ARP). ARP uses chirped pulses, which need to be measured and deterministically adjusted in order to effectively use them. Therefore, the majority of this chapter will focus on the chirp and how to determine and adjust it, with the help of simulations and later with measurements.

### **4.2. Chirp**

A chirped signal is a signal of which the frequency changes over time. For example, the frequency of a linearly chirped signal  $f(t)$  would be described by

$$f(t) = ct + f_0 \quad (4.1)$$

where  $f_0$  is the starting frequency at  $t = 0$  and  $c$  is the chirpiness. A linear chirped sinusoidal wave is depicted in figure 4.1.

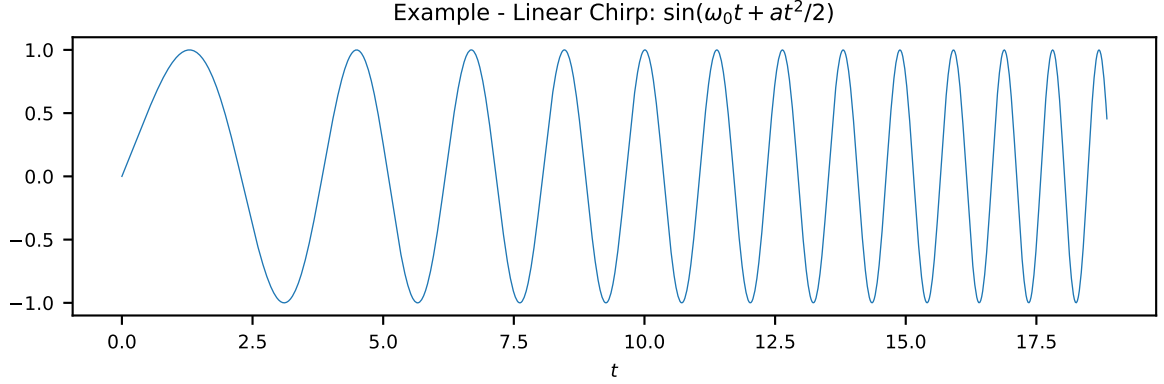


Figure 4.1.: A chirped sinusoidal wave which increases in frequency over time.

As this chapter is concentrated on exciting QDs with frequency-chirped pulses, the mathematical description of chirped laser pulses will now be discussed. The electric field of a laser  $E(t)$  has the shape

$$E(t) \sim \text{Re} \left( f^{1/2}(t) \cdot \exp(-i\omega t - i\phi(t)) \right) \quad (4.2)$$

with the central frequency  $\omega$  and the linear chirp  $\phi(t)$ .

Depending on the laser either a Gaussian or a hyperbolic secant describes the pulse shape more accurately [33, 34]

- Gaussian pulse:

- Pulse shape of

$$f_{gauss}(t) = \left( \frac{A_{gauss}}{\sqrt{2 \cdot \pi \cdot \tau_0 \cdot \tau}} \exp\left(-\frac{t^2}{2 \cdot \tau^2}\right) \right)^2 \quad (4.3)$$

with the normalization constant  $A_{gauss}$ , the pulse duration  $\tau_0$ , the central frequency  $\omega$  and the chirp coefficient  $\alpha$ .

- Linear chirp of

$$\phi_{gauss}(t) = \frac{a_{gauss} t^2}{2} \quad (4.4)$$

where  $\tau = \sqrt{\alpha^2/\tau_0^2 + \tau_0^2}$  characterizes the chirped pulse length and  $a = \alpha/(\alpha^2 + \tau_0^4)$  is the frequency chirp rate.

- Secant pulse:

- Pulse shape of

$$f_{secant}(t) = A_{secant} \cdot \operatorname{sech}^2\left(\frac{t}{\tau_0}\right) = A_{secant} \cdot \left(\frac{2}{\exp\left(\frac{t}{\tau_0}\right) + \exp\left(-\frac{t}{\tau_0}\right)}\right)^2 \quad (4.5)$$

with the normalization constant  $A_{secant}$ , the pulse duration  $\tau_0$ , the central frequency  $\omega$  and the chirp coefficient  $\alpha$ .

- Linear chirp of

$$\phi_{secant}(t) = \alpha_{secant} \left(\frac{t}{\tau_0}\right)^2 \quad (4.6)$$

The following discussion will assume a Gaussian laser shape as described by equation (4.3) and (4.4). A simulation for  $E$  is plotted in figure 4.2 for different chirp parameters  $\alpha$  suitable to display examples for strong and weak chirps. As can be seen there, the chirp parameter strongly influences the shape of the electric field. If  $E$  could be measured directly, the chirp could be easily estimated. That this not feasible for our use case, as our Ti:Sa laser can produce laser pulses as short as 100 fs and response times of photodiodes and oscilloscopes are in the best case in the order of 200 fs. This means they cannot even measure the duration of these ultrashort pulses let alone resolve the pulse shape.

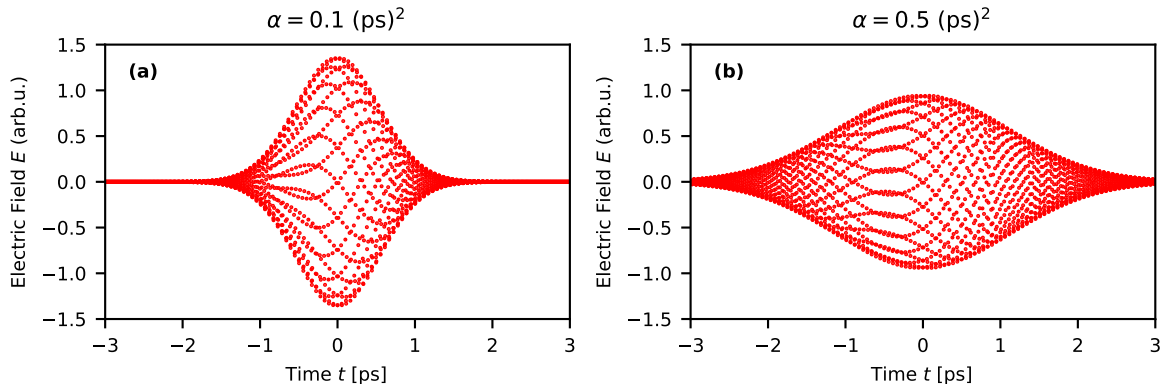


Figure 4.2.: Electric field  $E$  of Gaussian laser pulse of pulse duration  $\tau_0 = 0.5 \text{ ps}$  for chirp of (a)  $\alpha = 0 \text{ ps}^2$  and (b)  $\alpha = 0.5 \text{ ps}^2$

### 4.3. Measuring the chirp with interferometric autocorrelation

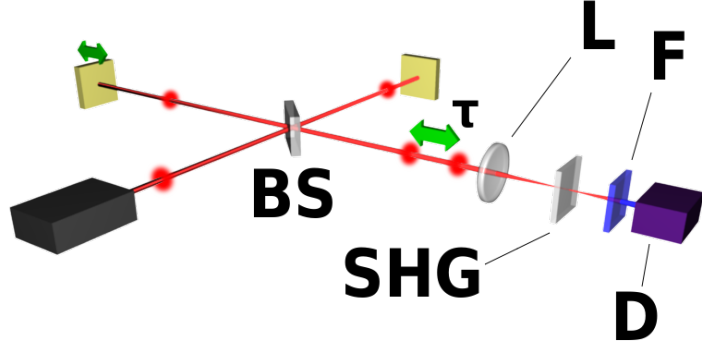


Figure 4.3.: Schematics of an interferometric autocorrelator, where **L** is a converging lens, **SHG** a second-harmonic generation crystal, **BS** a beam splitter,  $\tau$  the interval between two pulses, **D** the detector and **F** a spectral filter to block the fundamental wavelength [35].

In order to estimate the pulse width  $\tau_0$  interferometric autocorrelation (IAC) is used. Basically, a nonlinear crystal is added to a Michelson interferometer in order to generate a signal governed by

$$I_M(\tau) = \int_{-\infty}^{+\infty} \langle |(E(t) + E(t - \tau))^2|^2 \rangle dt. \quad (4.7)$$

and plotted in figure 4.4 [36]. Here  $\langle \rangle$  denotes averaging over fast oscillations of the electric field.

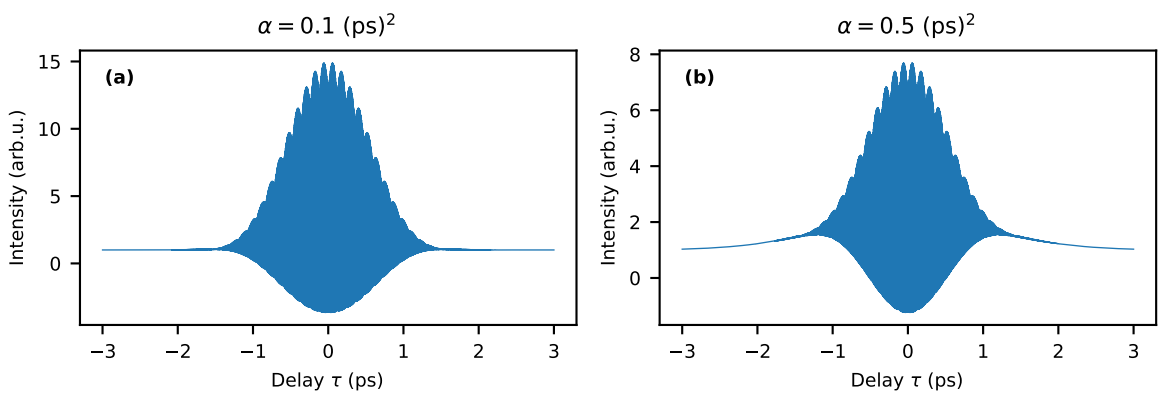


Figure 4.4.: Intensity of IAC of a Gaussian laser pulse of pulse duration  $\tau_0 = 0.5$  ps with applied MOSAIC filter for chirp of (a)  $\alpha = 0 \text{ ps}^2$  and (b)  $\alpha = 0.5 \text{ ps}^2$

Under the use of equation 4.2, equation (4.7) can be expanded to

$$I(\tau) = 1 + 2 \int f(t)f(t+\tau)dt + \int f(t)f(t+\tau) \cos(2\omega\tau + 2\Delta\phi)dt \\ + 2 \int f^{1/2}(t)f^{3/2}(t+\tau) \cos(\omega\tau + \Delta\phi)dt + 2 \int f^{3/2}(t)f^{2/2}(t+\tau) \cos(\omega\tau + \Delta\phi)dt \quad (4.8)$$

where  $\Delta\phi(t, \tau) = \phi(t + \tau) - \phi(t)$  and  $\int f(t)dt = 1$ .

As can be seen in figure 4.4 the chirp parameter  $\alpha$  has hardly any measurable influence on the resulting signal. However, certain modifications to the IAC signal introduced by Hirayama and Sheik-Bahae [34] make it much more sensitive to the temporal chirp. It is called modified-spectrum autointerferometric correlation (MOSAIC) and performs the following transformations on the IAC spectrum: the  $\omega$  terms are eliminated and the  $2\omega$  term is doubled. The MOSAIC signal is then described by

$$I_M(\tau) = 1 + 2 \int f(t)f(t+\tau)dt + 2 \int f(t)f(t+\tau) \cos(2\omega\tau + 2\Delta\phi)dt. \quad (4.9)$$

When the MOSAIC filter is applied on the data shown in figure 4.4 it results in a signal as shown in figure 4.5. Here the influence of the chirp is clearly visible in the lower envelope.

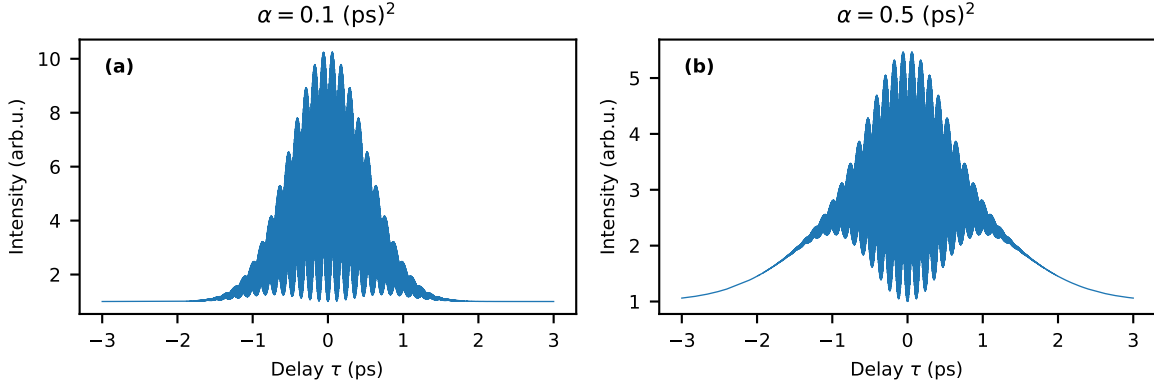


Figure 4.5.: Intensity of IAC of a Gaussian laser pulse of pulse duration  $\tau_0 = 0.5$  ps with applied MOSAIC filter for chirp of (a)  $\alpha = 0 \text{ ps}^2$  and (b)  $\alpha = 0.5 \text{ ps}^2$

#### 4. Entangled photon generation using adiabatic rapid passage with frequency-chirped pulses

---

The points of the lower envelope can be obtained by determining the local minima of the signal as shown in figure 4.6.

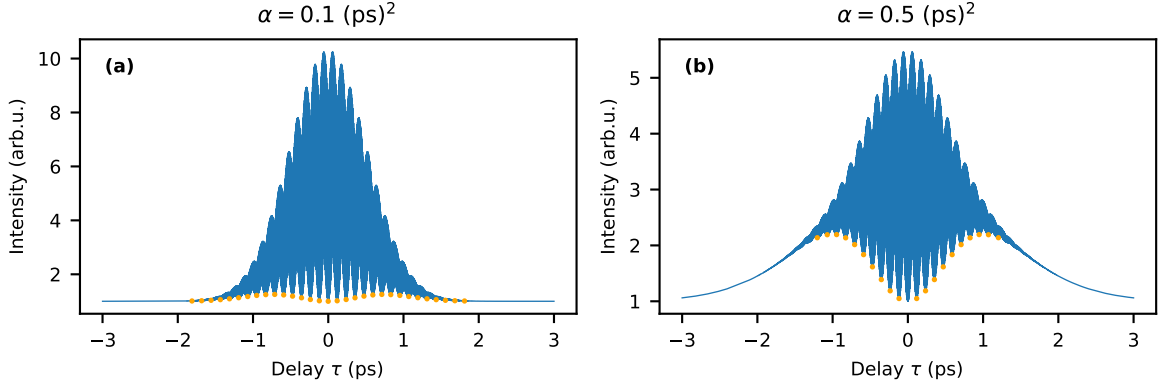


Figure 4.6.: Intensity of IAC of a Gaussian laser pulse of pulse duration  $\tau_0 = 0.5$  ps with applied MOSAIC filter for chirp of (a)  $\alpha = 0 \text{ ps}^2$  and (b)  $\alpha = 0.5 \text{ ps}^2$ . The orange dots are results of a numerical peak finder algorithm, executed in order to find local minima.

The lower bound (minima envelope) of the MOSAIC trace can be derived by use of standard textbook procedure [37]

$$S_{\text{MOSAIC}}^{\min}(\tau) = 1 + 2 \cdot g(\tau) - 2 \cdot [g_s^2(\tau) + g_c^2(\tau)]^{1/2} \quad (4.10)$$

with

$$g(\tau) = \int f(t)f(t+\tau)dt \quad (4.11)$$

$$g_s(\tau) = \int f(t)f(t+\tau)\sin(2\Delta\phi)dt \quad (4.12)$$

$$g_c(\tau) = \int f(t)f(t+\tau)\cos(2\Delta\phi)dt \quad (4.13)$$

The points of the lower envelope determined before can now be fitted in order to obtain the chirp parameter  $\alpha$  as shown in figure 4.7. It is visible that the fitted values of  $\alpha$  correspond to the expected values.

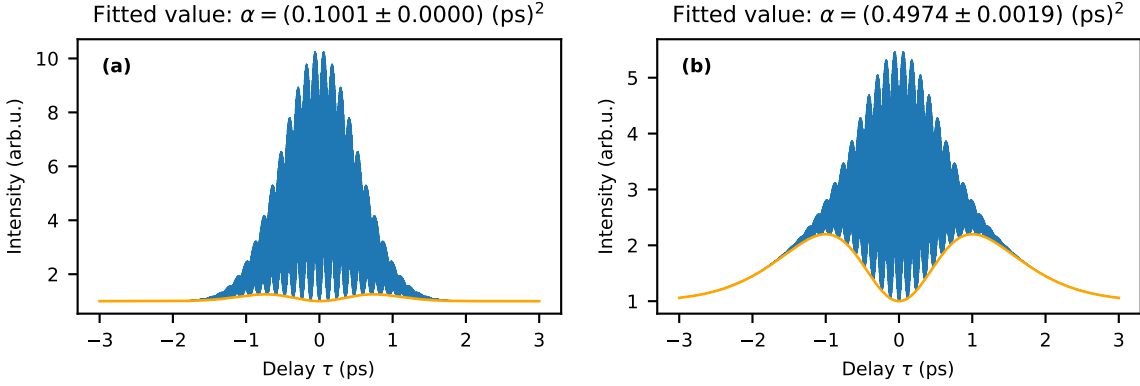


Figure 4.7.: Intensity of IAC of a Gaussian laser pulse of pulse duration  $\tau_0 = 0.5$  ps with applied MOSAIC filter for chirp of (a)  $\alpha = 0 \text{ ps}^2$  and (b)  $\alpha = 0.5 \text{ ps}^2$ . The orange line is a fit for the lower envelope of the MOSAIC signal in order to obtain  $\alpha$ .

## 4.4. Deterministically adjusting the chirp with a pulse expander

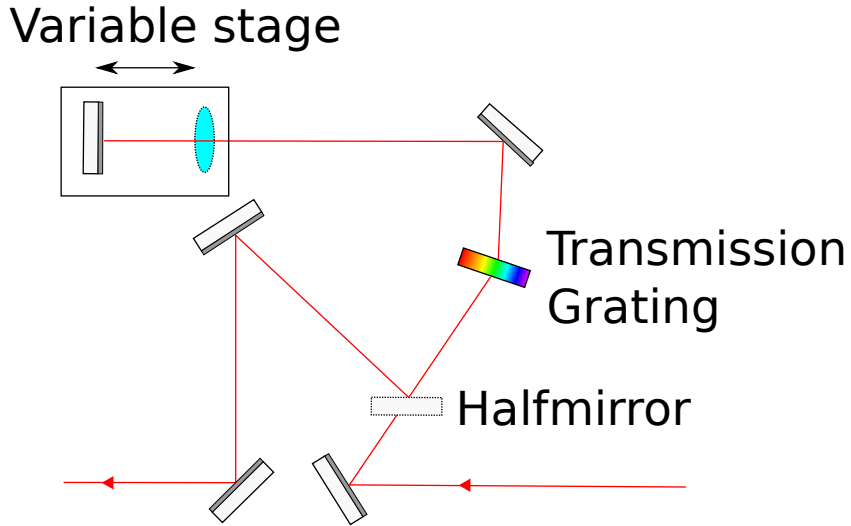


Figure 4.8.: Scheme of a folded pulse expander as described by Martinez [38]. The light enters on the right side, passes the halfmirror, and enters the system of transmission grating, lens and mirrors. Afterwards it hits the halfmirror and exits on the left hand.

In the optimal case the chirp of the pulse can be deterministically adjusted in order to most efficiently excite the QD via adiabatic rapid passage (going to be introduced in section 4.5). Grating compressors

as discussed by Martinez [38] were originally used to compensate the broadening effect fibers have on pulses. However, together with a telescope they have the inverse effect and can be used to induce a chirp. A setup like this is sketched in figure 4.8 and it will in future references in this work be called *pulse expander*. Its main elements are the transmission grating and the lens and this folded setup uses a mirror after the lens in order to need only one lens and mirror. The accumulated group velocity dispersion can be adjusted by varying the optical distance  $d$  between the focal plane of the lens and the transmission grating and is described by

$$\frac{d^2\Phi}{d\omega^2} = k\beta^2 2d \quad (4.14)$$

where  $\beta$  is a value depending on the parameters of the grating and the lens.

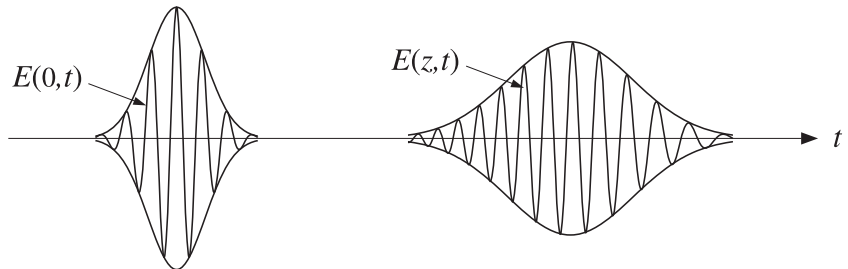


Figure 4.9.: Influence of group velocity dispersion for example inside a fiber on a Gaussian pulse [39]

As can be seen in figure 4.9, a group velocity dispersion has a similar effect on a Gaussian pulse as a chirp. In fact, the frequency chirp rate  $a_{gauss}$  introduced in equation (4.4) can be put into relation with it by: [39]

$$a_{gauss} = \frac{\frac{d^2\Phi}{d\omega^2}}{\tau_0^4 + \left(\frac{d^2\Phi}{d\omega^2}\right)^2} \quad (4.15)$$

## 4.5. Adiabatic rapid passage

One way to invert the QD from the ground state  $|G\rangle$  to the biexciton state  $|XX\rangle$  is by exciting it with a narrow-band laser pulse of constant centre frequency, which is equals to half of the ground state biexciton transition frequency. As described in equation (2.16), if the pulse area  $\theta = \pi$ , a population inversion from the  $|G\rangle$  state to the  $|XX\rangle$  occurs. However, the  $\pi$ -pulse method is not a generally robust scheme. In order to ensure the inversion, precise control of the field intensity is required [33]. Adiabatic rapid passage (ARP) with frequency chirped is a much more robust alternative to this Rabi-flopping scheme. Here, the frequency of the laser signal is swept through resonance, starting slightly above or

below the resonance frequency. The biexciton state can be populated with nearly perfect efficiency [33] if the process is performed adiabatically [40]

$$\Omega_0 \gg |d/dt\omega(t)| \quad (4.16)$$

where  $\Omega_0$  is the peak Rabi frequency and  $\omega(t)$  is the center frequency of the laser pulse.

In figure 4.10 simulations in order to determine the final biexciton occupation for different biexciton binding energies  $\Delta$  by Glässl et al. [33] are presented. Here, a linearly-chirped Gaussian laser pulse as discussed in section 4.2 was assumed.

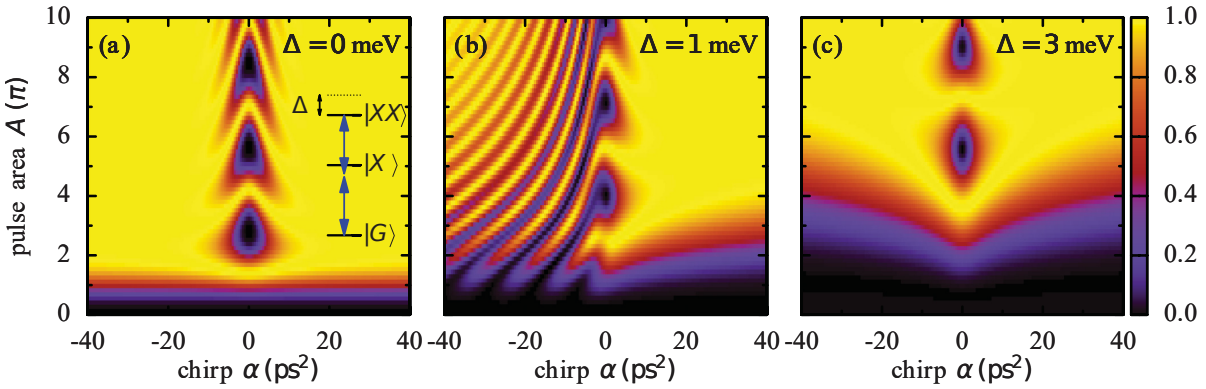


Figure 4.10.: Final biexciton occupation after chirped Gaussian pulse of pulse duration  $\tau_0 = 2$  ps. It is plotted vertically as a function of the original pulse area  $A$  and vertically as a function of the chirp  $\alpha$  for biexciton binding energies of (a)  $\Delta = 0$ , (b) 1, and (c) 3 meV [33].

The central frequency is chosen so that for  $\alpha = 0$  it resonates to ground state biexciton transition, which is sketched in figure 4.10. For  $\alpha = 0$  Rabi oscillations are visible and its period depends strongly on the biexciton binding energy  $\Delta$ . However, for  $\alpha \gg 0$  biexciton preparation becomes insensitive to small variations to the pulse area  $A$  as long it exceeds a certain threshold. This is therefore the regime which would be the most suitable to work in. In the case of  $\alpha < 0$  this insensitivity does not appear for moderate values of  $\Delta$  as can be seen in figure 4.10(b).

## 4.6. Measurements and discussion

As discussed in the sections above, the final goal is to excite QD via ARP. The first step to do that is to determine the chirp of a laser pulse which only passed the pulse shaper with the IAC. Here laser pulse of only  $\tau_0 = 344$  fs was used as the IAC can not resolve fine enough details for greater  $\tau_0$ . Even though broader peaks will be necessary in order to excite the QD with ARP, this is not a problem as the equivalent chirp can be calculated for greater  $\tau_0$  with equation (4.4).

Afterwards, a signal was measured where an additional pulse expander inserted as discussed in section 4.4 and sketched in figure 3.1. The comparison between these two is shown in figure 4.11. Compared to the simulations in figure 4.4 it is visible that the IAC of the laser pulse without the pulse expander fits the expected shape well, while the one with the pulse expander does not. Possible reasons could be that the chirp is too high for the model used in the simulation to work or that the pulse expander introduces side effects not considered in the simulation.

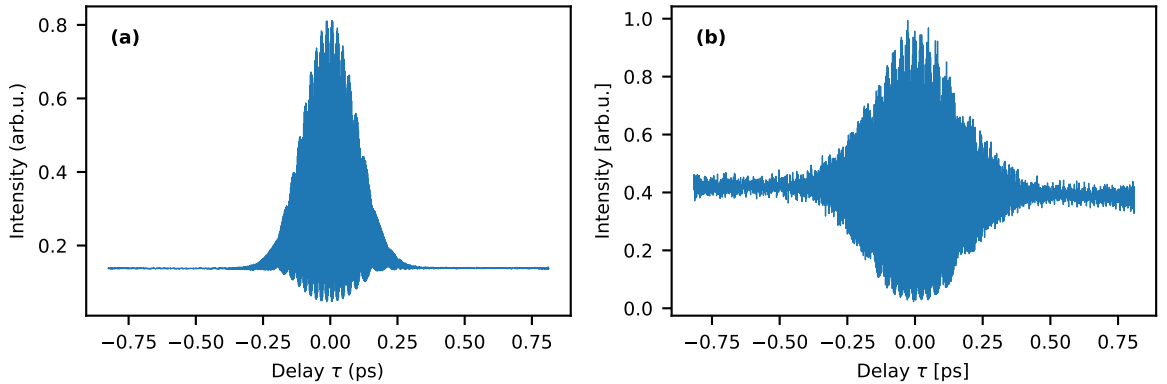


Figure 4.11.: Measured IAC of Ti:Sa Laser without (a) and with (b) pulse expander before the autocorrelator.

The same signals after applying the MOSAIC filter are shown in figure 4.12. It is visible that the lower envelopes in figure 4.12(a) and 4.12(b) do not resemble the expected ones in figure 4.5. As the laser signal without pulse expander was assumed to be relatively unchirped, it is already unexpected that the lower envelope differs that much from a constant line at zero intensity. One explanatory approach could be that the laser was already chirped to begin with. However, this would not explain why the shape of the lower envelope differs from the characteristic one of the simulation.

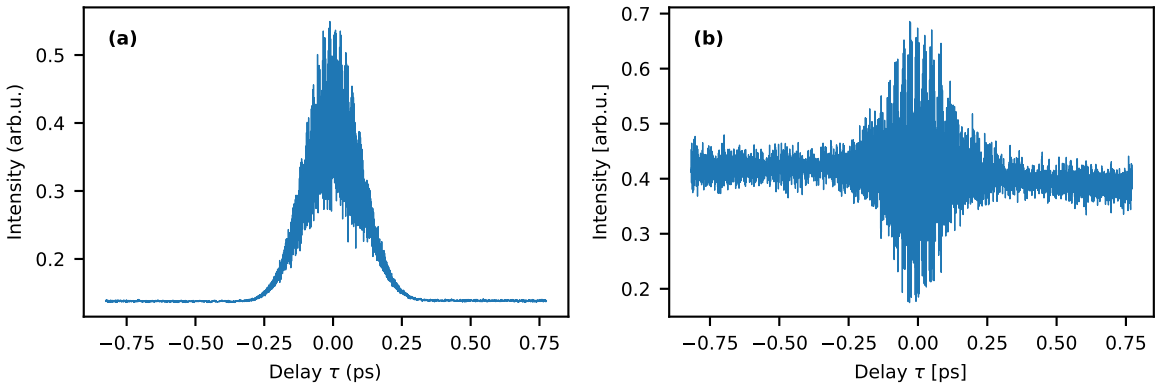


Figure 4.12.: Measured IAC of Ti:Sa Laser with applied MOSAIC filter without (a) and with (b) pulse expander before the autocorrelator.

The next step would have been to deterministically excite the QD with ARP. However it might be advisable to repeat the same procedure with another ultrashort pulsed laser beforehand in order to rule out that our laser is already heavily chirped to begin with. Alternatively, ARP with the pulse expander can be attempted without measuring the chirp first and iteratively adjusting the lens-grating distance until the optimum is reached.



# 5. Building up a scanning Fabry-Pérot interferometer from scratch

## 5.1. Introduction and motivation

The Fabry Pérot interferometer (FPI) is an optical resonator developed by Charles Fabry and Alfred Pérot. An incoming light beam will only be transmitted through the resonator consisting of two semi-transparent mirrors if it fulfills the resonance condition.[41]. The resonance frequencies can be changed by adjusting the mirror distance. By measuring the intensity at the output of the FPI, this can be used to resolve fine features of an electromagnetic spectrum, like e.g. the emitted light from the exciton-groundstate radiative decay described in section 2.3. The following chapter introduces basics of electromagnetic radiation, describes simulations performed to size the components of the FPI and displays measurement techniques used to obtain the resolved exciton spectrum.

## 5.2. Transverse modes of electromagnetic radiation

### 5.2.1. Gaussian beam

In this chapter, light beams are described by the wave picture according to Meschede [42]. They fulfil the Maxwell equations and therefore their electric field  $\mathbf{E}(\mathbf{r}, t)$  fulfills the wave equation

$$\left( \nabla^2 - \frac{1}{c^2} \frac{\partial^2}{\partial t^2} \right) \mathbf{E}(\mathbf{r}, t) = 0. \quad (5.1)$$

Along the propagation direction  $z$  a light beam behaves similarly to a plane wave with constant amplitude  $A_0$  which is a known solution to the wave equation (5.1)

$$E(z, t) = A_0 e^{-i(\omega t - kz)}. \quad (5.2)$$

## 5. Building up a scanning Fabry-Pérot interferometer from scratch

---

However, far from its source light is expected to behave like a spherical wave

$$E(\mathbf{r}, t) = A_0 \frac{e^{-i(\omega t - \mathbf{k}\mathbf{r})}}{|\mathbf{k}\mathbf{r}|}. \quad (5.3)$$

To get a better understanding of the propagation of light, only paraxial (near the z-axis) parts of the spherical wave are considered. Additionally, the wave is split into its longitudinal (z-axis) part and its transversal part and beams with axial symmetry are assumed, which only depend on a transversal coordinate  $\rho$ . Under these circumstances  $\mathbf{k}\mathbf{r}$  can be replaced with  $kr$  and because of  $\rho \ll r, z$  the Fresnel approximation can be applied:

$$E(\mathbf{r}) = \frac{A(\mathbf{r})}{|\mathbf{k}\mathbf{r}|} e^{ik\mathbf{r}} \simeq \frac{A(z, \rho)}{kz} \exp\left(i \frac{k\rho^2}{2z}\right) e^{ikz} \quad (5.4)$$

with  $r = \sqrt{z^2 + \rho^2} \simeq z + \rho^2/2z$ .

Equation (5.4) resembles the plain wave in equation (5.2), with the spacial phase transversal modulated by  $\exp(ik\rho^2/2z)$ . Another spherical wave solution can be obtained by applying the following replacement ( $z_0$  is a real number)

$$z \rightarrow q(z) = z - iz_0 \quad (5.5)$$

with  $q(z)$  as the complex beam parameter. Thereby, the fundamental (or TEM<sub>00</sub>) Gaussian mode has been constructed

$$E(z, \rho) \simeq \frac{A_0}{kq(z)} \exp\left(i \frac{k\rho^2}{2q(z)}\right) e^{ikz}. \quad (5.6)$$

The electric and magnetic fields of Gauss modes are transversal to its propagation direction. These waveforms are called transversal electric and magnetic modes with indices  $(m, n)$ . Its fundamental solution is the TEM<sub>00</sub>-Mode, which is the most important one and will therefore be examined in more detail in the rest of this subsection.

By executing the replacement  $q(z) \rightarrow z - iz_0$  explicitly the equation (5.6) can be expressed as

$$\frac{1}{q(z)} = \frac{z + iz_0}{z^2 + z_0^2} = \frac{1}{R(z)} + i \frac{2}{k\omega^2(z)}, \quad (5.7)$$

with new variables  $z_0$ ,  $R(z)$  and  $\omega(z)$  being introduced. With the decomposition of the Fresnel factors into real and imaginary part, two factors can be identified: one complex phase factor, which describes the curvature of the wavefronts and a real factor, which describes the envelope of the beam. Therefore, the exponential in equation (5.6) becomes

$$\exp\left(i \frac{k\rho^2}{2q(z)}\right) \rightarrow \exp\left(i \frac{k\rho^2}{2R(z)}\right) \exp\left(-\left(\frac{\rho}{\omega(z)}\right)^2\right) \quad (5.8)$$

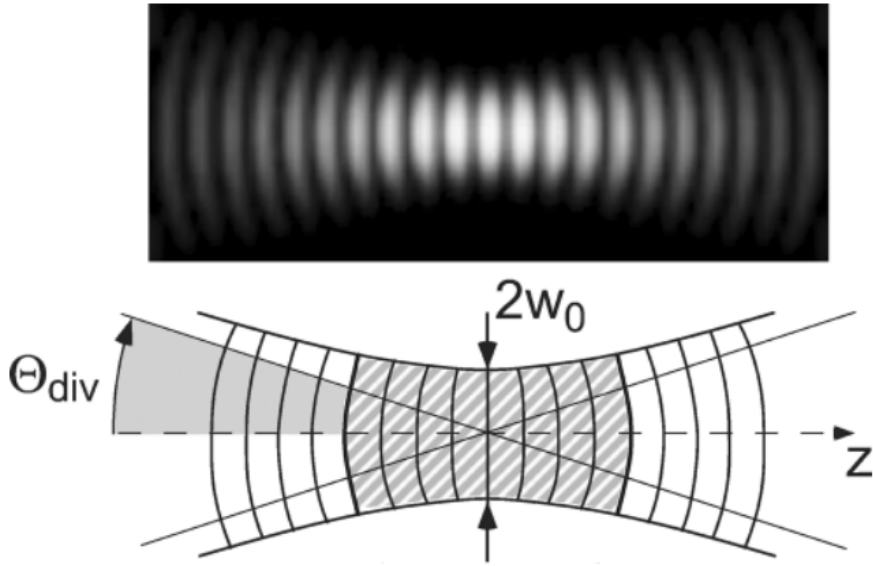


Figure 5.1.: A Gaussian beam near its beam waist. Near the center they resemble plan wave fronts, while outside they converge towards spherical wave fronts. They Rayleighzone is shaded at the lower part of the figure.[42]

For a proper description of a Gaussian beam as shown in figure 5.1 the following parameters have to be introduced

- **Evolving radius of curvature  $R(z)$ :**

$$R(z) = z(1 + (z_0/z)^2) \quad (5.9)$$

- **Beam waist  $2\omega_0$ :**

$$\omega_0^2 = \lambda z_0 / \pi \quad (5.10)$$

The beam waist  $2\omega_0$  or beam radius  $\omega_0$  describes the smallest beam cross section at  $z = 0$ . If the wave propagates inside a medium with the refractive index  $n$ ,  $\lambda$  has to be replaced with  $\lambda/n$ . The cross section of the beam waist is then  $\omega_0^2 = \lambda z_0 / (\pi n)$ .

A Gaussian beam can be completely characterized at every point  $z$  on the beam axis either with the parameter couple  $(\omega_0, z_0)$  or alternatively with the real and imaginary part of  $q(z)$ . The parameters of the Gaussian beam are transformed by the ray transfer matrix

$$q_{out} = \frac{Aq_{in} + B}{Cq_{in} + D} \quad (5.11)$$

with the parameters  $A, B, C, D$  determined by the optical element transforming the Gaussian beam described by  $q_{in}$ .

### 5.2.2. Higher Gauss modes

The wave equation (5.1) can be simplified by only allowing monochromatic waves with harmonic time dependence

$$\mathbf{E}(\mathbf{r}, t) = \text{Re} \left( \mathbf{E}(\mathbf{r}) e^{-i\omega t} \right). \quad (5.12)$$

With  $\omega^2 = c^2 \mathbf{k}^2$ , the *Helmholtz equation* can be deduced, which only depends on the location  $\mathbf{r}$

$$(\nabla^2 + \mathbf{k}^2) \mathbf{E}(\mathbf{r}) = 0. \quad (5.13)$$

In favor of a formal treatment of the Gaussian modes, the Helmholtz equation is split into its transversal and longitudinal contributions,

$$\nabla^2 + k^2 = \frac{\partial^2}{\partial z^2} + \nabla_T^2 + k^2 \quad \text{with} \quad \nabla_T^2 = \frac{\partial}{\partial x^2} + \frac{\partial}{\partial y^2}. \quad (5.14)$$

Additionally, the electric field  $E$  of equation (5.4) is inserted into the Helmholtz equation. It is also assumed that the amplitude  $A$  only changes slowly in the order of the wavelength,

$$\frac{\partial}{\partial z} A = A' \ll kA, \quad (5.15)$$

which allows the approximation

$$\frac{\partial^2}{\partial z^2} A e^{ik\rho^2/(2z)} \frac{e^{ikz}}{kz} \simeq (2ikA' - k^2 A) e^{ik\rho^2/(2z)} \frac{e^{ikz}}{kz}, \quad (5.16)$$

and results in the *paraxial Helmholtz equation*,

$$\left( \nabla_T^2 + 2ik \frac{\partial}{\partial z} \right) A(\rho, z) = 0. \quad (5.17)$$

The fundamental solution is the TEM<sub>00</sub> mode in equation (5.6). Examples of higher modes can be found in figure 5.2.

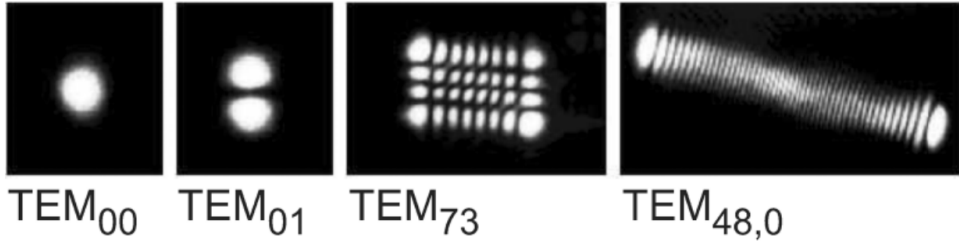


Figure 5.2.: Gaussian modes higher order of a simple Ti-sapphire laser. The asymmetry of the high modes are caused by technical inaccuracies of the resonator elements (mirrors, laser crystal).

## 5.3. Fundamentals of Fabry-Pérot interferometers

### 5.3.1. Resonator losses

For the following discussion of the FPI, a two-mirror-resonator with the reflecting surfaces facing each other and air as medium in between is assumed. The theoretical foundation is provided by the work of Ismail et al. [43].

The time the light needs for one roundtrip is given by

$$t_{RT} = \frac{2l}{c} \quad (5.18)$$

where  $l$  is the geometrical length of the resonator and  $c$  is the speed of light in air.

The photon-decay time  $\tau_c$  of the interferometer is then given by

$$\frac{1}{\tau_c} = -\frac{\ln(R_1 \cdot R_2)}{t_{RT}} \quad (5.19)$$

where  $R_1$  and  $R_2$  are the corresponding intensity reflectivities of the mirrors.

The number of photons at frequency  $\nu$  inside the resonator is described by the differential rate equation

$$\frac{d}{dt} \varphi(t) = -\frac{1}{\tau_c} \varphi(t). \quad (5.20)$$

With a number  $\varphi_s$  of photons at  $t = 0$  the integration gives

$$\varphi(t) = \varphi_s e^{-t/\tau_c} \quad (5.21)$$

### 5.3.2. Resonance frequencies, free spectral range and spectral line shapes

The round-trip phase shift at frequency  $\nu$  is given by

$$2\phi(\nu) = 2\pi\nu t_{RT} = 2\pi\nu \frac{2l}{c} \quad (5.22)$$

where  $\phi(\nu)$  is the single-pass phase shift between the mirrors.

Resonances are visible for frequencies  $\nu$  at which the light interferes constructively after one round trip. Two adjacent resonance frequencies differ in their round trip phase shift by  $2\pi$ . Hence, the free spectral range  $\Delta\nu_{FSR}$ , the frequency difference between two adjacent resonance frequencies, can be calculated from equation (5.22)

$$2\Delta\phi_{FSR} = 2\pi \quad (5.23)$$

$$\Rightarrow 2\pi\Delta\nu_{FSR} \frac{2l}{c} = 2\pi \quad (5.24)$$

$$\Rightarrow \Delta\nu_{FSR} = \frac{c}{2l} \quad (5.25)$$

According to equation (5.21) the number of photons decays with the photon-decay time  $\tau_c$ . With  $E_{q,s}$  representing the initial amplitude, the electric field at  $\nu_q$  is given by

$$E_q(t) = \begin{cases} E_{q,s} \cdot e^{i2\pi\nu_q t} \cdot e^{-t/(2\tau_c)} & t \geq 0 \\ 0 & t < 0 \end{cases}. \quad (5.26)$$

The Fourier transformation of the electric field can be expressed as

$$\tilde{E}_q(\nu) = \int_{-\infty}^{\infty} E_q(t) e^{-i2\pi\nu t} dt = E_{q,s} \int_0^{\infty} e^{[1/(2\tau_c) + i2\pi(\nu - \nu_q)]t} dt = E_{q,s} \frac{1}{(2\tau_c)^{-1} + i2\pi(\nu - \nu_q)}. \quad (5.27)$$

The normalized spectral line shape per unit frequency is then given by

$$\tilde{\gamma}_q(\nu) = \frac{1}{\tau_c} \left| \frac{\tilde{E}_q(\nu)}{E_{q,s}} \right|^2 = \frac{1}{\tau_c} \left| \frac{1}{(2\tau_c)^{-1} + i2\pi(\nu - \nu_q)} \right|^2 = \frac{1}{\tau_c} \frac{1}{(2\tau_c)^{-2} + 4\pi^2(\nu - \nu_q)^2} \quad (5.28)$$

$$= \frac{1}{\pi} \frac{1/(4\pi\tau_c)}{1/(4\pi\tau_c)^2 + (\nu - \nu_q)^2} \quad (5.29)$$

with  $\int \tilde{\gamma}_q(\nu) d\nu = 1$ .

By defining the full-width-at-half-maximum linewidth (FWHM)  $\Delta\nu_c$ ,  $\tilde{\gamma}_q(\nu)$  can be obtained

$$\Delta\nu_c = \frac{1}{2\pi\tau_c} \Rightarrow \tilde{\gamma}_q(\nu) = \frac{1}{\pi} \frac{\Delta\nu_c/2}{(\Delta\nu_c/2)^2 + (\nu - \nu_q)^2}. \quad (5.30)$$

Afterwards the Cauchy lines are normalized so that the peak is at unity

$$\gamma_{q,L}(\nu) = \frac{\pi}{2} \Delta\nu_c \tilde{\gamma}_q(\nu) = \frac{(\Delta\nu_c)^2}{(\Delta\nu_c)^2 + 4(\nu - \nu_q)^2} \quad (5.31)$$

with  $\gamma_{q,L}(\nu_q) = 1$ .

### 5.3.3. Airy distribution of Fabry-Pérot interferometers

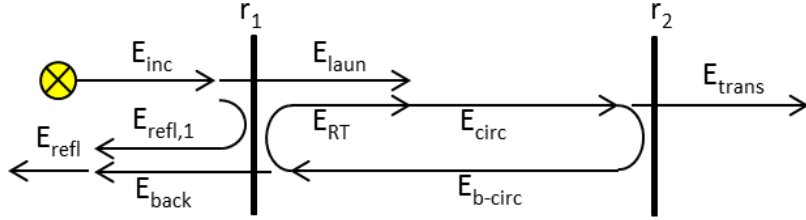


Figure 5.3.: FPI with electric field mirror reflectivities  $r_1$  and  $r_2$ . Indicated in this figure are the electric fields resulting from an incoming  $E_{inc}$ , the reflected field  $E_{refl,1}$  and transmitted field  $E_{laun}$ .  $E_{circ}$  and  $E_{circ,b}$  circulate inside the resonator, resulting in  $E_{RT}$  after one round-trip.  $E_{back}$  is the backwards transmitted field.[44]

The response of the FPI is calculated with the circulating-field approach [43], where a steady-state is assumed.  $E_{circ}$  is the result of  $E_{laun}$  interfering with  $E_{RT}$ .  $E_{laun}$  is the transmission of the incoming light  $E_{inc}$  and  $E_{RT}$  is  $E_{circ}$  after one round-trip in the resonator, i.e., after the outcoupling losses of mirror 1 and 2. Therefore, the field  $E_{circ}$  can be calculated from  $E_{laun}$  by

$$E_{circ} = E_{laun} + E_{RT} = E_{laun} + r_1 r_2 e^{-i2\phi} E_{circ} \Rightarrow \frac{E_{circ}}{E_{laun}} = \frac{1}{1 - r_1 r_2 e^{-i2\phi}} \quad (5.32)$$

where  $r_1$  and  $r_2$  are the electric-field reflectivities of mirror 1 and 2.

The generic Cauchy distribution only considers light inside the mirrors and is defined as

$$A_{circ} = \frac{I_{circ}}{I_{laun}} = \frac{|E_{circ}|^2}{|E_{laun}|^2} = \frac{1}{|1 - r_1 r_2 e^{-i2\phi}|^2} = \frac{1}{(1 - \sqrt{R_1 R_2})^2 + 4\sqrt{R_1 R_2} \sin^2(\phi)} \quad (5.33)$$

by using

$$\begin{aligned} |1 - r_1 r_2 e^{-i2\phi}|^2 &= |1 - r_1 r_2 \cos(2\phi) + i r_1 r_2 \sin(2\phi)|^2 = [1 - r_1 r_2 \cos(2\phi)]^2 + r_1^2 r_2^2 \sin^2(2\phi) \\ &= 1 + R_1 R_2 - 2\sqrt{R_1 R_2} \cos(2\phi) = (1 - \sqrt{R_1 R_2})^2 + 4\sqrt{R_1 R_2} \sin^2(\phi) \end{aligned}$$

and additionally  $R_i = r_i^2$  and  $\cos(2\phi) = 1 - 2\sin^2(\phi)$ .

## 5. Building up a scanning Fabry-Pérot interferometer from scratch

---

Commonly, light is sent through the FPI. Therefore the following sections will use the Airy distribution  $A'_{trans}$  described by

$$A'_{trans} = \frac{I_{trans}}{I_{inc}} = \frac{I_{circ} \cdot (1 - R_2)}{I_{laun} / (1 - R_1)} = (1 - R_1)(1 - R_2) A_{circ} = \frac{(1 - R_1)(1 - R_2)}{(1 - \sqrt{R_1 R_2})^2 + 4\sqrt{R_1 R_2} \sin^2(\phi)} \quad (5.34)$$

with  $\phi = \frac{\pi v}{\Delta\nu_{FSR}}$ .

$A'_{trans}$  is displayed in figure 5.4 for  $R_1 = R_2$ . The peak value at one of its resonance frequencies calculates as follows

$$\max(A'_{trans}) = \frac{(1 - R_1)(1 - R_2)}{(1 - \sqrt{R_1 R_2})^2} \stackrel{R_1=R_2}{=} 1. \quad (5.35)$$

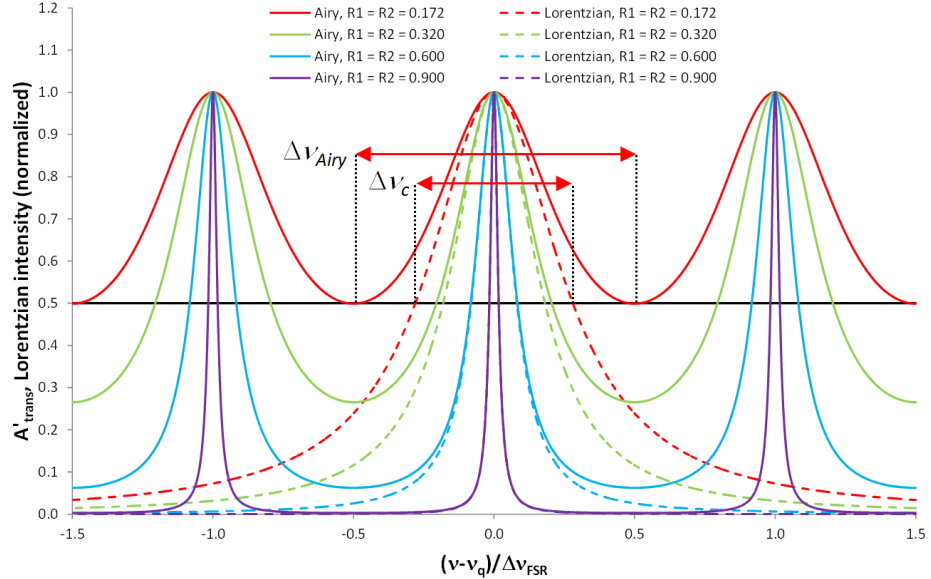


Figure 5.4.: Airy distribution  $A'_{trans}$  as described in equation (5.34) compared to the Cauchy lines  $\gamma_{q,L}$  as described in equation (5.31) [44].

### 5.3.4. Airy linewidth and finesse

The airy linewidth is defined as the FWHM of  $A'_{trans}$ . It can be set in relation with the free spectral range  $\Delta\nu_{FSR}$  and the mirror reflectivities as follows.

$A'_{trans}$  decreases to half of its peak value at  $A'_{trans}(v_q)/2$  when the phase shift  $\phi$  changes by the amount

$\Delta\phi$  so that the denominator of  $A'_{trans}$  in equation (5.34) is twice as big

$$\left(1 - \sqrt{R_1 R_2}\right)^2 = 4\sqrt{R_1 R_2} \sin^2(\Delta\phi) \quad (5.36)$$

$$\Rightarrow \Delta\phi = \arcsin\left(\frac{1 - \sqrt{R_1 R_2}}{2\sqrt[4]{R_1 R_2}}\right) \quad (5.37)$$

With equation (5.22) and (5.25), the phase shift can be expressed as

$$\phi = \frac{\pi\nu}{\Delta\nu_{FSR}} \quad (5.38)$$

$$\Rightarrow \Delta\phi = \frac{\pi(\Delta\nu_{Airy}/2)}{\Delta\nu_{FSR}}. \quad (5.39)$$

Therefore, with equation (5.37) and (5.39) the FWHM linewidth is given by

$$\Delta\nu_{Airy} = \Delta\nu_{FSR} \frac{2}{\pi} \arcsin\left(\frac{1 - \sqrt{R_1 R_2}}{2\sqrt[4]{R_1 R_2}}\right). \quad (5.40)$$

The finesse of the Airy distribution of a FPI is defined as

$$F_{Airy} := \frac{\Delta\nu_{FSR}}{\Delta\nu_{Airy}} = \frac{\pi}{2} \left[ \arcsin\left(\frac{1 - \sqrt{R_1 R_2}}{2\sqrt[4]{R_1 R_2}}\right) \right]^{-1} \quad (5.41)$$

and is therefore only dependent on the mirror reflectivities  $R_1$  and  $R_2$ .

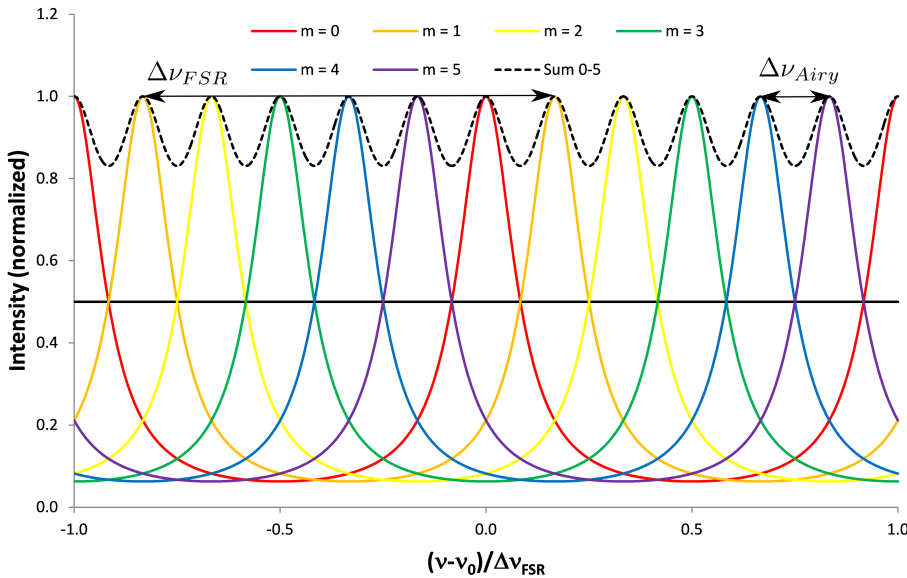


Figure 5.5.: Demonstration of the physical meaning of the Airy finesse  $F_{Airy}$ . The coloured lines are Airy distributions created by light at distinct frequencies  $\nu_m$ , while scanning the resonator length. When the light occurs at frequencies  $\nu_m = \nu_q + m\Delta\nu_{Airy}$ , the adjacent Airy distributions are separated from each other by  $\nu_{Airy}$ , therefore fulfilling the Taylor criterion. Since in this example  $F_{Airy} = 6$  exactly six peaks fit inside the free spectral range. As can be seen in the figure the Airy finesse  $F_{Airy}$  quantifies the maximum number of peaks that can be resolved [44].

## 5. Building up a scanning Fabry-Pérot interferometer from scratch

The Airy finesse is the determining property when it comes to the spectral resolution of the FPI. This can be made visible by comparing its message with the Taylor criterion for the resolution of two adjacent peaks. The Taylor criterion proposes that two spectral lines are resolvable when the separation of the maxima is greater than the FWHM. As displayed in figure 5.5, the Airy finesse is equal to the number of Airy distributions originating from light at certain frequencies  $\nu_m$  which do not overlap at a point higher than half of their maxima. Hence, the Airy finesse describes the spectral resolution in a way that is consistent with the Taylor criterion.

### 5.3.5. Mode matching and spatial filtering

One fundamental challenge of Fabry Pérot interferometry is how to efficiently couple an incident beam of light into a given mode of the resonator. The following discussion is based on the work of Yariv, Yeh, and Yariv [45] and Meschede [42].

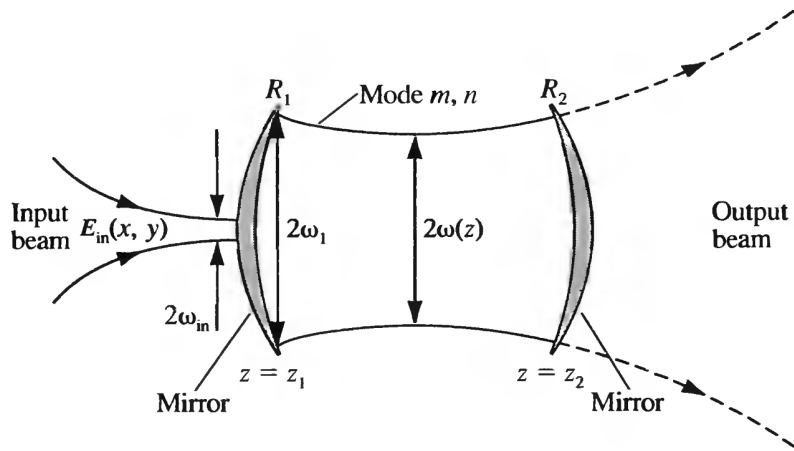


Figure 5.6.: Incident monochromatic beam of light exciting transverse mode  $m, n$  of a resonator [45]

In sketched with figure 5.6, an input beam  $E_{in}$  propagates into the resonator and potentially excite its modes  $E_{mn}(x, y)$ , where  $m, n$  are the transverse mode integers of the Gaussian beam of the optical resonator. Since  $E_{mn}(x, y)$  describes a complete orthogonal set of wavefunctions they satisfy

$$\iint E_{mn}(x, y) E_{m'n'}^*(x, y) dx dy = 0 \quad \text{unless } m = m' \text{ and } n = n'. \quad (5.42)$$

and

$$E_{in}(x, y) = \sum_{mn} a_{mn} E_{mn}(x, y) \quad (5.43)$$

where  $a_{mn}$  are constants. By multiplying both sides of equation (5.43) with  $E_{mn}^*$ , integrating over the whole  $x$ - $y$ -plane and using equation (5.42), the following expression can be obtained

$$a_{mn} = \frac{\iint E_{in}(x,y)E_{mn}^*(x,y)dxdy}{\iint E_{mn}(x,y)E_{mn}^*(x,y)dxdy} \quad (5.44)$$

The efficiency of coupling an incident field into a spatial mode  $E_{mn}$  is defined as

$$\eta_{mn} = \frac{\text{Power coupled into mode } mn}{\text{Total incident power}} = \frac{\iint |a_{mn}E_{mn}(x,y)|^2 dxdy}{\iint |E_{in}(x,y)|^2 dxdy}. \quad (5.45)$$

By inserting equation (5.44) into equation (5.45) the following expression can be obtained

$$\eta_{mn} = \frac{|\iint E_{in}(x,y)E_{mn}^*(x,y)dxdy|^2}{\iint |E_{in}(x,y)|^2 dxdy \cdot \iint |E_{mn}(x,y)|^2 dxdy}. \quad (5.46)$$

From equation (5.46) can be deduced that for an input beam with the *same* spatial dependency as the mode to be excited

$$E_{in}(x,y) \sim E_{mn}(x,y) \quad (5.47)$$

all of the incident power goes into  $E_{mn}$ , i.e.  $\eta_{mn} = 1$  and all other  $\eta_{m'n'}$  are zero. Usually, the fundamental TEM<sub>00</sub> mode is desired and equation (5.46) implies that a pure Gaussian beam excites only the fundamental mode and the interferometer will then irradiate a pure Gaussian beam as well. In practise, additional measures are necessary such as matching the radius of curvature by Gaussian beam focusing.

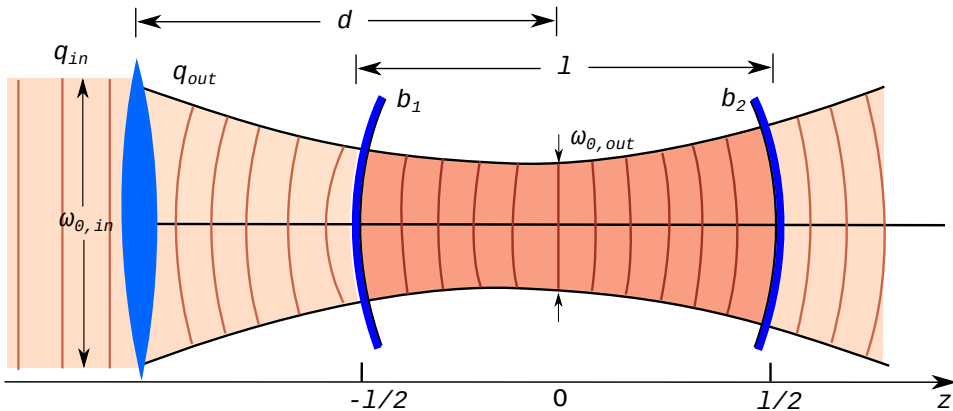


Figure 5.7.: Mode matching of an Gaussian beam into a Fabry Pérot interferometer. Incoming Gaussian beam described by  $q_{in}$  transformed by a lens into a Gaussian beam described by  $q_{out}$ . The parameters  $b_1$  and  $b_2$  describe the radii of the two mirrors.

In order to match the radius of curvature of the incoming Gaussian beam with the radius of curvature of the resonator a lens is inserted as depicted in figure 5.7. Light with a beam waist of  $\omega_{01}$  gets

focused into the resonator. Transformations by thin lenses can be described with the ray transfer matrix introduced in subsection 5.2.1:

$$\begin{pmatrix} A & B \\ C & D \end{pmatrix} = \begin{pmatrix} 1 & 0 \\ \frac{-1}{f} & 1 \end{pmatrix} \quad (5.48)$$

with  $f$  as the wavelength of the lens. The incoming beam described by  $q_{in}$  is transformed by the lens into a beam described by  $q_{out}$  according to equation (5.10) and (5.11)

$$q_{in} = z + i \frac{\pi n \omega_{0,in}^2}{\lambda} \quad \text{and} \quad q_{out} = \frac{q_{in}}{q_{in} \cdot \frac{-1}{f} + 1} = z + i \frac{\pi n \omega_{0,out}^2}{\lambda} \quad (5.49)$$

with  $n \approx 1$  for air. Together with equation (5.10) the following relation can be deduced

$$\omega_{0,out}^2 = \frac{\omega_{0,in}^2}{\left(1 - \frac{z}{f}\right)^2 + \left(\frac{\pi \omega_{0,in}}{\lambda f}\right)^2}. \quad (5.50)$$

The radii of curvature have to match. For given mirrors (described by  $R_{mirror}$ ) and lens (described by  $f$ ) the input beam waist has to be adjusted according to equation (5.9) and (5.10)

$$R_{mirror} \stackrel{!}{=} R_{gauss}(z = l/2) \quad (5.51)$$

$$R_{mirror} \stackrel{!}{=} \frac{l}{2} \left(1 + \left(\frac{2z_{0,out}}{l}\right)^2\right) \quad (5.52)$$

$$R_{mirror} \stackrel{!}{=} \frac{l}{2} \left(1 + \left(\frac{2\omega_{0,out}^2 \pi}{l \lambda}\right)^2\right). \quad (5.53)$$

Inserting equation (5.53) into equation (5.50) results in the condition for mode matching

$$R_{mirror} = \frac{l}{2} \left(1 + \left(\frac{\frac{2\omega_{0,in}^2 \pi}{l \lambda}}{\left(\left(1 - \frac{z}{f}\right)^2 + \left(\frac{\pi \omega_{0,in}}{\lambda f}\right)^2\right) l \lambda}\right)^2\right). \quad (5.54)$$

One way to further suppress higher modes is *spatial filtering*. It can be seen in figure 5.2 that the effective area of a mode increases with its order ( $m, n$ ). Figure 5.8 shows one way to suppress higher modes consisting of a focusing lens and a pin hole which diameter matches the one of the TEM<sub>00</sub> mode.

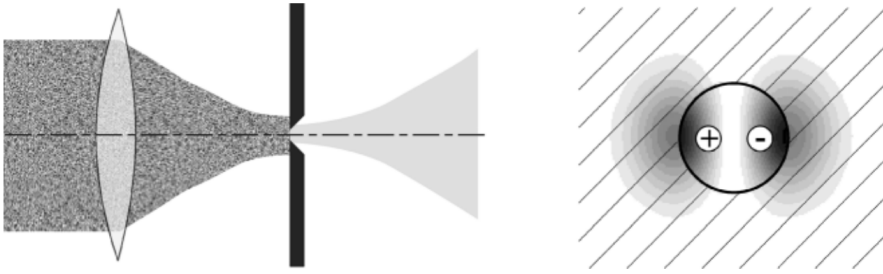


Figure 5.8.: Spatial filtering of Gauss modes. In front of the aperture, the beam consists of a superposition of multiple Gauss modes. In the example of TEM<sub>01</sub> is displayed how higher modes are suppressed by the aperture. [42]

### 5.3.6. Confocal setup

If the incoming beam would represent a perfect TEM<sub>00</sub> mode, spatial filtering would not be necessary and mode matching would not have to be done as precise. Unfortunately, this can not always be guaranteed and counteractions like mode matching and spatial filtering discussed in subsection 5.3.5 are tedious and error prone. Arranging the mirrors of an FPI into a confocal arrangement reduces the need for these measures. By giving up the ability to choose different free spectral ranges with a given pair of mirrors, the confocal setup liberates from mode matching considerations as the cavity is mode degenerated, i.e. the frequency of certain axial and transverse cavity modes are the same. The following discussion is based on the work of Hercher [46].

A quasi-monochromatic beam of wavelength  $\lambda_0$  is composed of transverse modes TEM<sub>mnq</sub>, where the subscripts  $m$  and  $n$  denote the amplitude distribution of the normal mode on a surface of constant phase and  $q$  the number of axial modes inside the resonator. Each of these modes resonates for mirror separations satisfying

$$l = \frac{\lambda_0}{2} \{q + (1 + m + n) \cos^{-1} [(1 - l/b_1)(1 - l/b_2)]^{1/2}\} \quad (5.55)$$

where the parameters  $b_1$  and  $b_2$  describe the radii of the two mirrors as can be seen in figure 5.7.

For the confocal setup  $l = b_1 = b_2$  justifies the approximation

$$l \approx \frac{\lambda_0}{2} [q + (1 + m + n)]. \quad (5.56)$$

The modes resonate at mirror separations of either

$$l = \frac{\lambda_0}{2}(p+1) \quad p \in \mathbb{N} \text{ and } (m+n) \text{ even}, \quad (5.57)$$

$$l = \frac{\lambda_0}{2}(p) \quad p \in \mathbb{N} \text{ and } (m+n) \text{ odd}. \quad (5.58)$$

If mode matching is not executed, it can be assumed that the incoming beam consists of an approximately equal number of even and odd transverse modes. The resonance cavity length  $l$  does not depend on  $n, m$  and  $q$  anymore but only on one integer  $p$ . The transversal modes are degenerate and fulfil

$$l = \frac{\lambda_0 p}{2}. \quad (5.59)$$

It can be additionally concluded from equation (5.59) that a change of  $\lambda_0/2$  in the mirror separation scans through one free spectral range.

## 5.4. Simulation

The goal in building up a scanning FPI is to resolve features of the emission spectra of GaAs quantum dots described in chapter 2. More precisely, it is intended to resolve the shape of the ZPL and the PSB. Equation 5.41 shows that the finesse is constant for a given pair of mirrors. If the spectrum to be resolved is broad, a higher free spectral range  $\Delta\nu_{FSR}$  has to be chosen, under the loss of resolution. If the spectrum contains fine details which need to be resolved, a lower  $\nu_{Airy}$  has to be chosen, which results in a lower free spectral range  $\Delta\nu_{FSR}$ . Hence, the thin ZPL and the broad PSB can not be resolved with the same setup. Instead, the mirror distances have to be adjusted and in the confocal setup discussed in subsection 5.3.6 the mirrors have to be changed as well.

The zero-phonon line is described with a Cauchy distribution

$$\Phi_{ZPL}(\lambda) = \frac{1}{\pi \cdot \Delta\lambda_{ZPL} \cdot 0.5 \left[ 1 + \left( \frac{\lambda - \lambda_{0,ZPL}}{\Delta\lambda_{ZPL} \cdot 0.5} \right)^2 \right]} \quad (5.60)$$

with  $\lambda_{0,zero}$  as the center wavelength and  $\Delta\lambda_{ZPL}$  as the spectral range of the zero-phonon line which can be found in table 2.1.

The phonon side band is described with a Gauss distribution

$$\Phi_{PSB}(\lambda) = \frac{1}{\sqrt{2 \cdot \pi \cdot \Delta\lambda_{PSB}^2}} \cdot \exp \left( -\frac{(\lambda - \lambda_{0,PSB})^2}{2 \cdot \Delta\lambda_{PSB}^2} \right) \quad (5.61)$$

#### 5.4. Simulation

with  $\lambda_{0,PSB}$  as the center wavelength and  $\Delta\lambda_{PSB}$  as the spectral range of the phonon side band which can be found in table 2.1 as well.

Together they describe the excitonic emission of the QD

$$\Phi_{dot}(\lambda) = \Phi_{ZPL}(\lambda) + \Phi_{PSB}(\lambda) \quad (5.62)$$

depicted in figure 5.9.

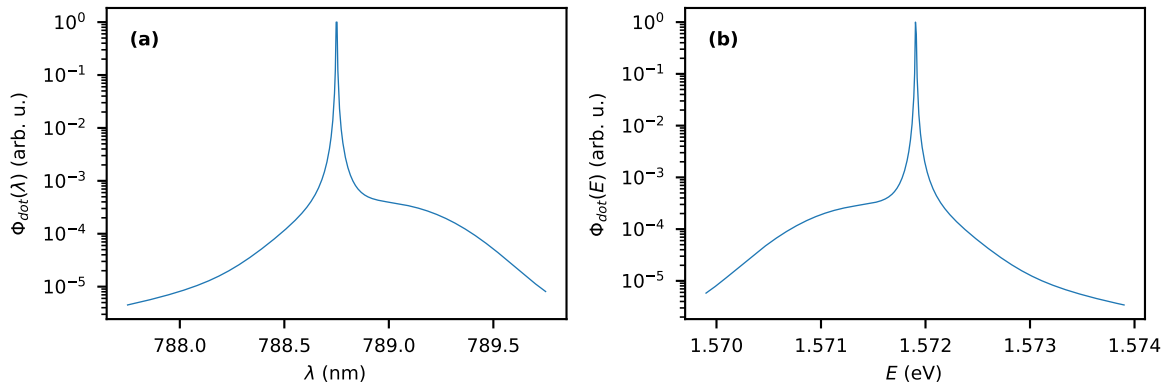


Figure 5.9.: Simulated exciton emission of a GaAs quantum dot plotted dependant on (a) the wavelength  $\lambda$  or (b) the energy  $E$ . The parameters can be found in table 2.1.

$\Phi_{dot}(E)$  is transmitted through the FPI. As discussed the mirror distance  $l$  is adjusted to a value which depends if a resolved ZPL or a resolved PSB is desired. A comparison of the FPI transmission  $A'_{trans}(E)$  described in equation 5.34 with  $R_1 = R_2 = 98\%$  and  $\Phi_{dot}(E)$  is shown in figure 5.10.

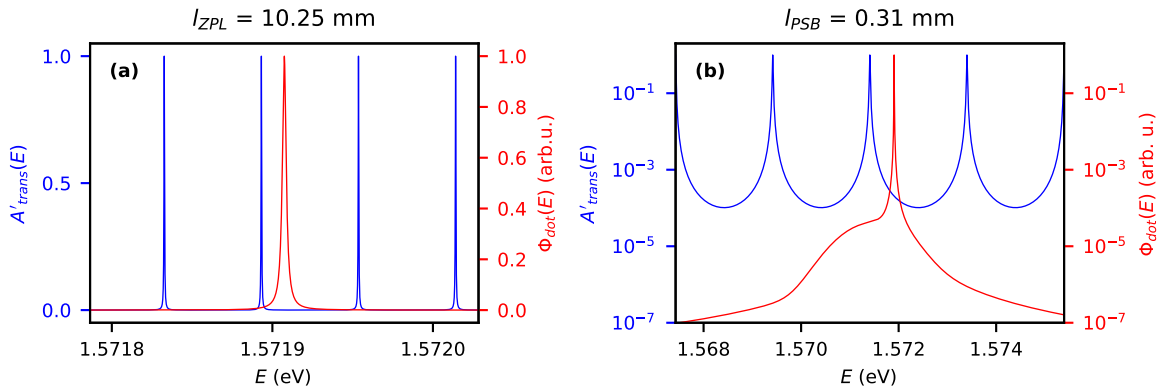


Figure 5.10.: Transmission of the FPI modes  $A'_{trans}$  compared to the exciton emission  $\Phi_{dot}(E)$  for (a) ZPL and (b) PSB.

## 5. Building up a scanning Fabry-Pérot interferometer from scratch

The FPI scans by continuously varying the mirror distance  $l$  with a certain stepsize  $\Delta l$  and measuring the output-photon-flux every time. This process is sketched in figure 5.11.

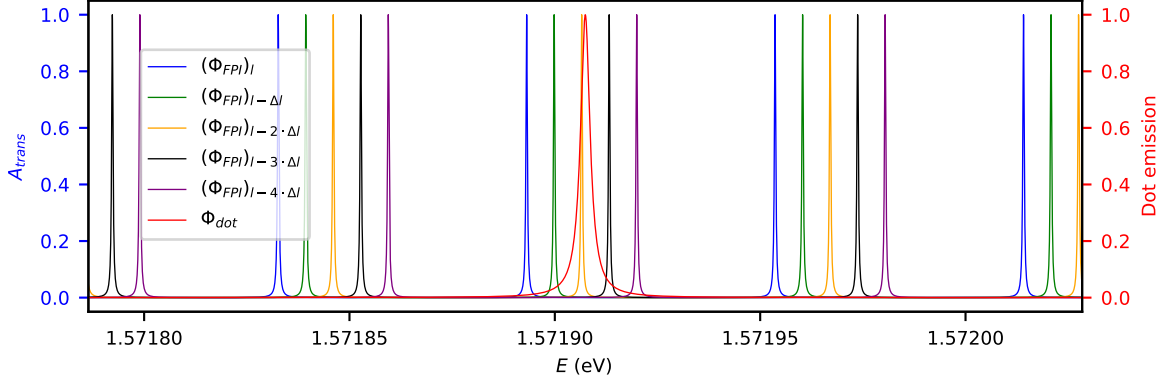


Figure 5.11.: Transmissions of the FPI modes  $A'_{trans}$  (blue) for different mirror distances  $l - m \cdot \Delta l$  with  $m \in \mathbb{N}$  compared to the exciton emission  $\Phi_{dot}(E)$  (red).

The unnormalized output-photon-flux of the scanning FPI is then described with the convolution of  $\Phi_{dot}(E)$  and  $A'_{trans}(E)$

$$\tilde{\Phi}_{FPI}(E) = \int_{E_0-n\cdot\Delta}^{E_0+n\cdot\Delta} \Phi_{dot}(E') A'_{trans}(E - E') dE' \quad (5.63)$$

with  $E_0$  as the central energy of the exciton emission line,  $\Delta$  as the free spectral range and  $2n = 4$  as the number of airy peaks considered for the numerical convolution.

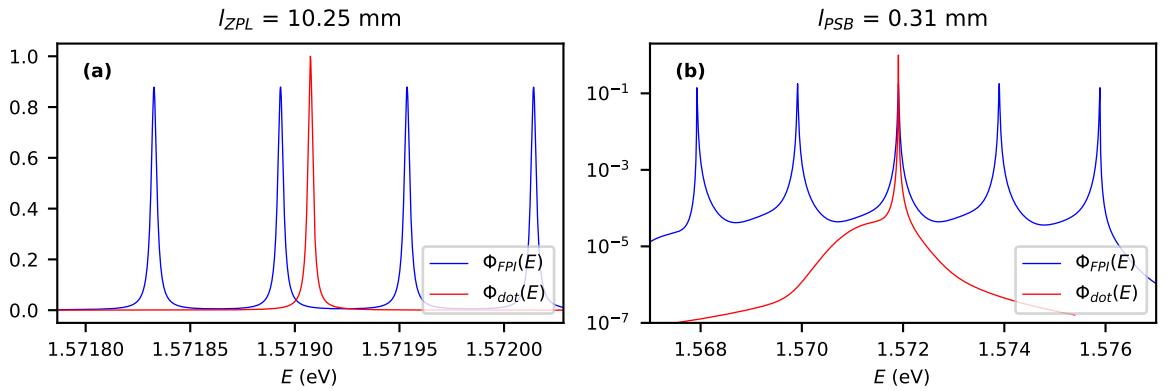


Figure 5.12.: Output-photon-flux of the scanning FPI  $\Phi_{FPI}(E)$  (blue) compared to the exciton emission  $\Phi_{dot}(E)$  (red) for (a) ZPL and (b) PSB.

$\tilde{\Phi}_{FPI}(E)$  can then be normalized with the integral of  $A'_{trans}(E)$  over the same range

$$\Phi_{FPI}(E) = \frac{\tilde{\Phi}_{FPI}(E)}{\int_{E_0-n\cdot\Delta}^{E_0+n\cdot\Delta} A'_{trans}(E) dE} \quad (5.64)$$

A comparison of  $\Phi_{FPI}(E)$  and  $\Phi_{dot}(E)$  is shown in figure 5.12.

From now on, only the ZPL-path is shown as no new information is gained by examining both. In order to estimate the accuracy of the scanning FPI, the FPI modes are shifted by  $\Delta E$  in order to overlap with  $\Phi_{dot}(E)$  as depicted in figure 5.13(a)

$$\bar{\Phi}_{FPI}(E) = \Phi_{FPI}(E - \Delta E). \quad (5.65)$$

Afterwards, the absolute difference between those two  $|\Phi_{dot}(E) - \Phi_{FPI}(E - \Delta E)|$  is calculated as shown in figure 5.13(b). Now the relative error of  $\Phi_{fabry,perot}(E)$  for the given parameters and compared to the actual excitonic QD emission can be calculated

$$\epsilon = \frac{\int_{E_0-\Delta/2}^{E_0+\Delta/2} |\bar{\Phi}_{FPI}(E) - \Phi_{dot}(E)| dE}{\int_{E_0-\Delta/2}^{E_0+\Delta/2} \Phi_{dot}(E) dE} \quad (5.66)$$

For the parameters in the ZPL path this gives  $\epsilon_{ZPL} = 10.57\%$ .

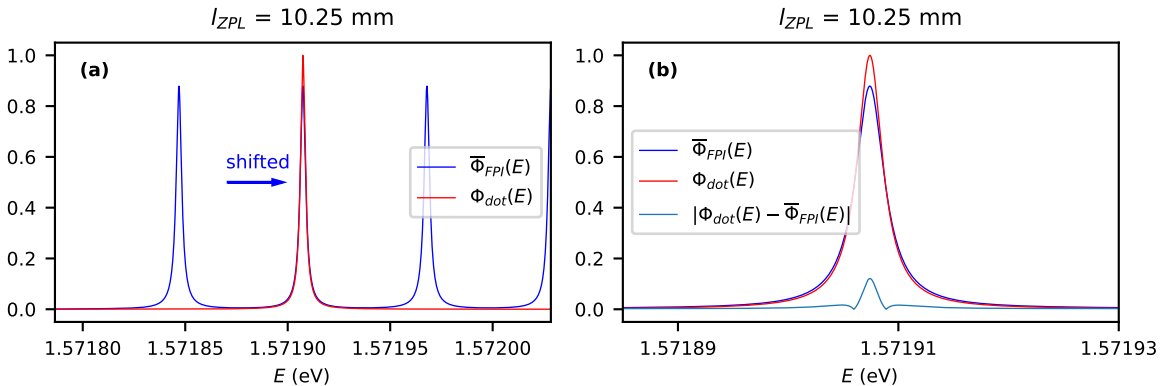


Figure 5.13.: In (a) the shifted output-photon-flux of the scanning FPI  $\bar{\Phi}_{FPI}(E)$  (blue) compared to the exciton emission  $\Phi_{dot}(E)$  (red) is displayed. In (b) the absolute difference between those two  $|\bar{\Phi}_{FPI}(E) - \Phi_{dot}(E)|$  (light blue) is additionally shown.

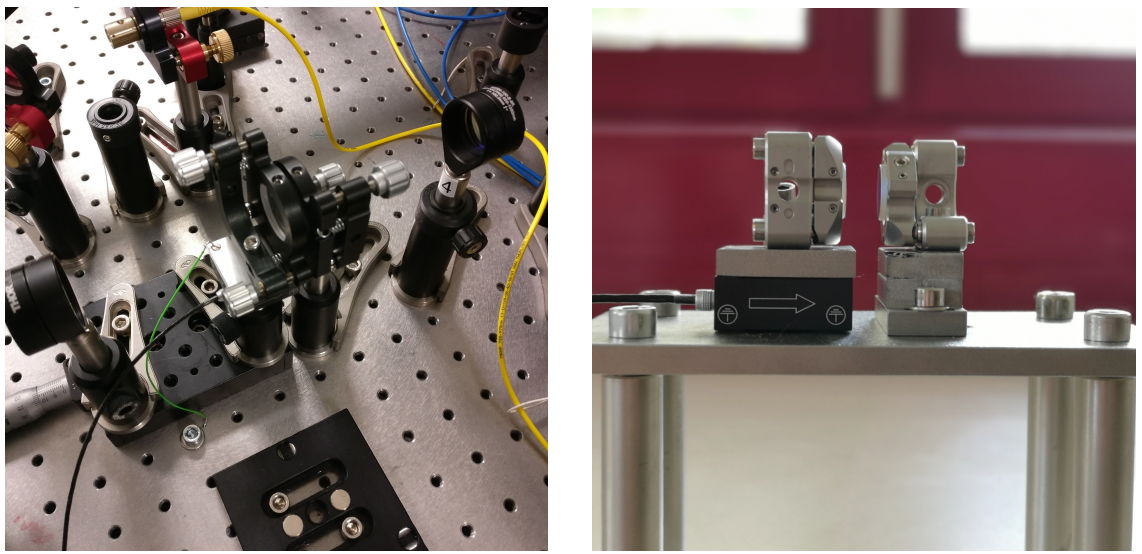
## 5.5. Setup and measurement

Multiple FPI setups were built up in order to test their suitability to resolve QD emission. The first version shown in figure 5.14a featured planar ( $r = 12.7 \text{ mm}$ ) mirrors, while their distance was coarsely

## 5. Building up a scanning Fabry-Pérot interferometer from scratch

---

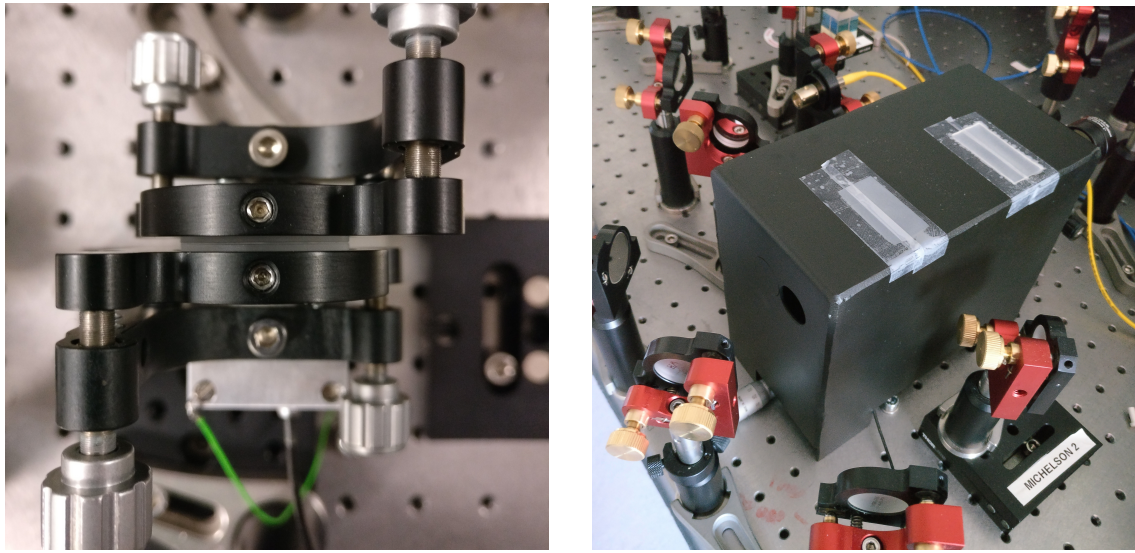
tunable with an adjustable platform and finely tunable with a piezoelectrical actuator. It used a lens in order to minimize the spot size at the FPI and a second lens with the same focal length in order to restore the original spot size. The mirror-distances are in the order of sub-micrometer as can be seen in figure 5.15a. This makes it difficult to ensure parallelism of the mirrors and also to estimate the mirror distances beforehand. In figure 5.15b, a casing is shown, built to block thermal fluctuations of the FPIs environment. However these measures proved to be not sufficient as the setup with planar mirrors turned out to be highly unstable.



(a) FPI on adjustable platform and finely tunable with a piezoelectrical actuator and planar mirrors of  $r = 12.7$  mm.  
 (b) FPI on molybdenum plate, coarsely tunable with elongated hole and finely tunable with a piezoelectrical actuator and planar mirrors of  $r = 6.35$  mm.

Figure 5.14.: Comparison between two setups where one uses bigger, planar mirrors and one uses smaller, planar-convex mirrors

The second version shown in figure 5.14b used smaller ( $r = 6.35$  mm), planar-convex mirrors and a ground plate made of molybdenum. Convex mirrors were implemented to allow mode-matching of the incoming beam. Molybdenum has a low thermal expansion coefficient, which is advantageous because of the FPIs sensitivity to mirror-distance-changes. This resulted in a stable FPI which was also adjustable for various free-spectral ranges. The measurements discussed in section 5.6 are obtained with this setup. However, the effort needed to mode-match for every measurement is too large to actually use it in further experiments. That is why the confocal setup will be used in the future, even though the freedom to adjust the free-spectral range is lost.



(a) Top view of FPI with planar mirrors and mirror distance of  
 $\approx 1 \mu\text{m}$ .

(b) Casing made of aluminium, built to block thermal fluctuations of  
 the FPIs environment.

Figure 5.15.: Top view of FPI and casing.

### 5.5.1. Scanning mode with fast photodiodes

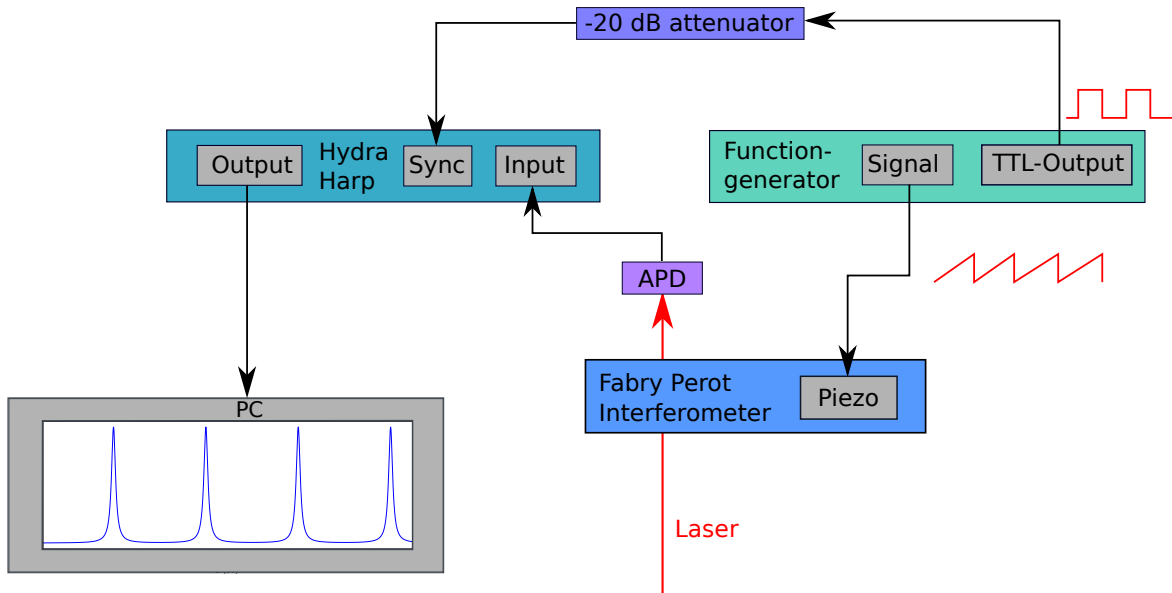


Figure 5.16.: Live avalanche photodiode setup with using a function generator driving the piezo actuator of the FPI and the sync input of the correlation hardware. APDs are used because of their speed, allowing to live-adjusting the FPI-parameters.

## 5. Building up a scanning Fabry-Pérot interferometer from scratch

---

Before the scanning FPI can be used to measure QD emission, it has to be aligned first usually with a (HeNe) laser. APDs are used for aligning the FPI as they are fast enough to measure the multiple free spectral ranges with a scanning frequency in the order of Hz. A function generator is used to drive the piezoelectrical actuator and the correlation hardware (here: Picoquant Hydralarp 400) correlates the measurements of the APD with the TTL-output of the function generator. The correlation hardware uses nuclear instrumentation module (NIM) as input, while the TTL-output uses Bayonet Neill-Concelman (BNC). Because of that a NIM-BNC converter had to be used in between. The complete setup is sketched in figure 5.16.

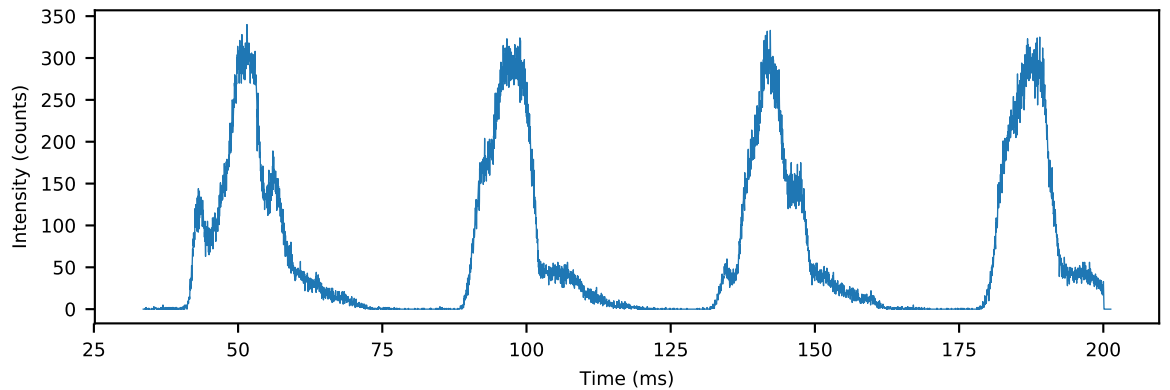


Figure 5.17.: Measurement of scanning FPI with APDs. The scanning frequency is 5 Hz and the range is 1  $\mu\text{m}$ . The measured finesse is  $\approx 5$  and the free spectral range corresponds to 280 nm.

Figure 5.17 shows the measurement of the scanning FPI with the APDs. The scanning frequency is 5 Hz and the range is 1  $\mu\text{m}$ . The measured finesse is  $\approx 5$  and the free spectral range corresponds to 280 nm. The stability for one snapshot as visible here appears good, however the modes shift visibly over a longer period of time.

### 5.5.2. Scanning mode with CCD

In order to obtain the spectral emission of the input signal, the FPI is used in the scanning mode. First the FPI has to be aligned, preferably with APDs and a (HeNe) laer. Afterwards, the signal of interest will be measured, in our case QD emission. The piezoelectric actuator moves step-wisely one of the mirror and after every step the output is recorded with the charge-coupled device (CCD). A minimal sketch of the setup is visible in figure 5.18.

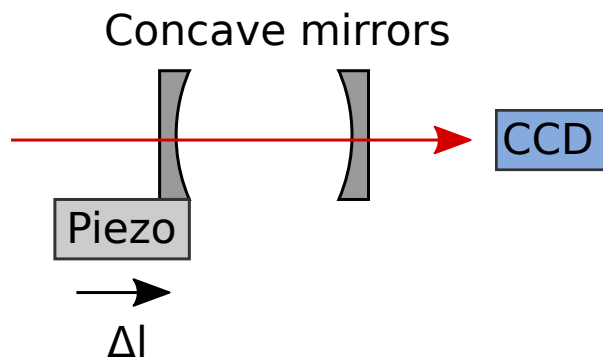


Figure 5.18.: Scanning Fabry Pérot interferometer with CCD

## 5.6. Measurements and discussion

In the following measurements the FPI was set up in the non-confocal mode and HeNe laser signals were used in order to align it. This involves for one setting the mirrors coming before the FPI so that the laser beam goes straight and centred through the FPI mirrors and then setting the FPI mirrors so that they are parallel and a single laser beam emerges as is shown in figure 5.19.

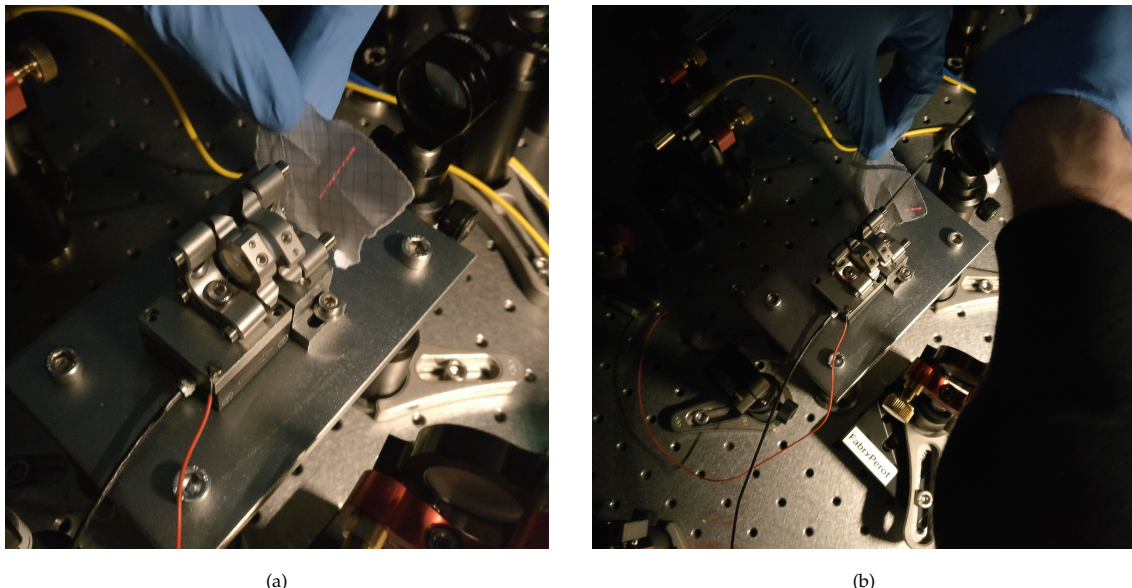


Figure 5.19.: Aligning the Fabry Pérot interferometer

Without spatial restriction strong TEM-modes of higher order are visible in figure 5.20(a). To counteract,

## 5. Building up a scanning Fabry-Pérot interferometer from scratch

---

a pinhole is inserted and adjusted which results in the measurement visible in figure 5.20(b).

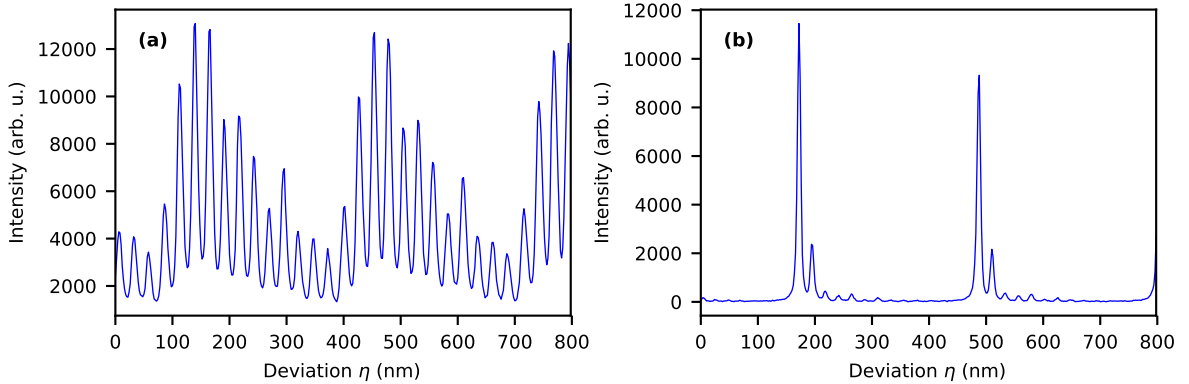


Figure 5.20.: Transmission measurement of FPI with ground mirror distance  $l \approx 2$  mm and HeNe laser. (a) was aligned without spatial filtering with a pinhole and (b) involved a pinhole.

Set up like this, the GaAs QD sample AS2o8 was measured. First a polarization map of the exciton was recorded in order to determine the FSS. This works by putting a polarizer and a  $\lambda/2$ -plate between the QD and the spectrometer. The  $\lambda/2$ -plate gets step-wisely rotated and the output will be recorded after every step. Because of the FSS of the QD the recorded centre energy of the exciton-groundstate emission will shift after step resulting in the plot shown in figure 5.21. From these data the FSS can be estimated which results in  $E_{FSS} = 24.42(39)$   $\mu\text{eV}$ .

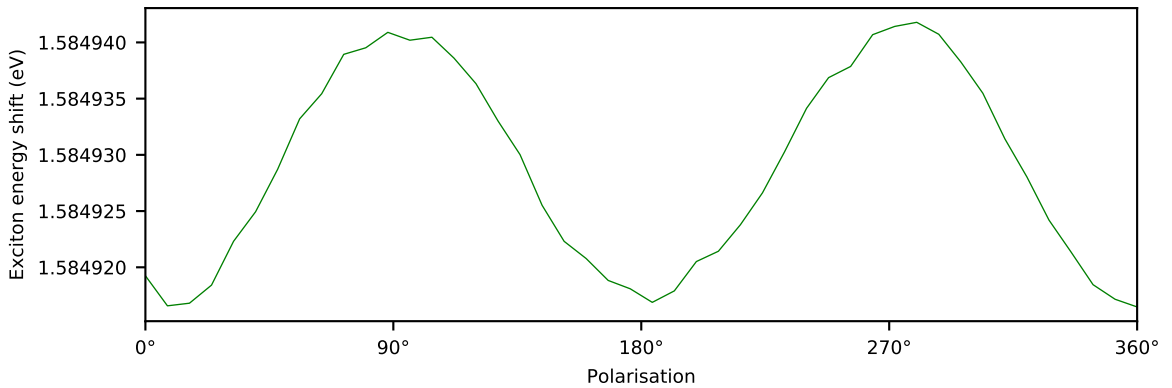


Figure 5.21.: Polarization map of exciton of QD in sample AS2o8.

Afterwards the output of the QD through the FPI was measured while the mirror distance was stepwisely changed which is shown in figure 5.22. The x-scale on the top of figure 5.22 was calculated

by correlating the distance between the two adjacent peaks with the FSS determined with the data of figure 5.21. For this QD results in a conversion between the deviations  $\eta = 1 \text{ nm} \hat{=} \zeta = 1.19(2) \mu\text{eV}$ .

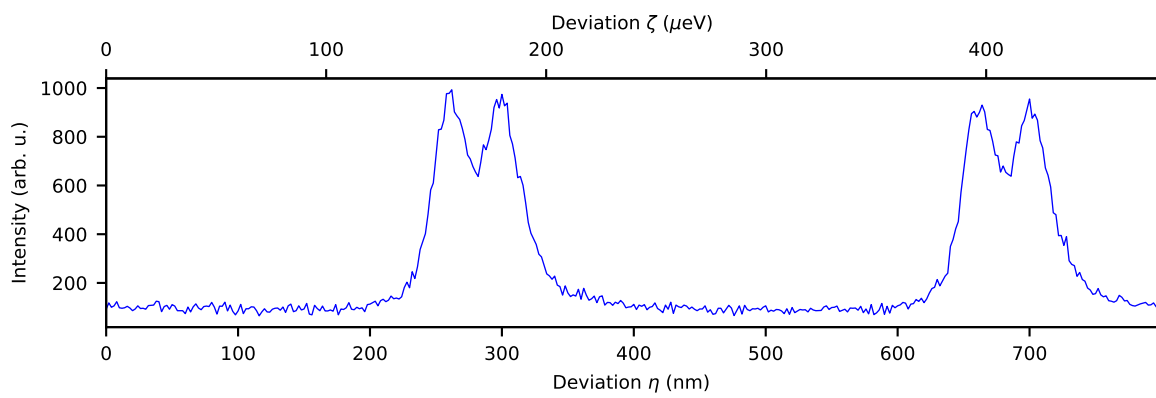


Figure 5.22.: Finestructure measurement of biexciton of QD in sample AS208 by passing thorough FPI and sweeping the mirror distance. Ground mirror distance was  $l \approx 2 \text{ mm}$ .

What does this comparison tell us?  
Did it fit the calculation?  
Where are the side peaks we saw in the HeNe measurement?  
What about the stability?  
Are there calculations, expected temperature drifts, etc. Are there differences between the expected Finesse and the measured one, and why? Is this expected?



## 6. Summary and outlook

The first topic presented in this thesis is entangled photon generation using ARP with frequency-chirped-pulses. The obstacles in quantifying the chirp just with IAC were discussed and one possible solution (MOSAIC) was presented. Finally, the pulse expander, used for deterministically adjusting the chirp, was introduced and measurements with and without the pulse expander were presented. However, the Ti:Sa laser used for these experiments later turned out to be heavily chirped to begin with, which made comparisons difficult. Additionally, it had to be sent away for reparation, which blocked further investigations. The next steps will be to investigate MOSAIC under different scenarios and then, if the chirp can be adjusted, attempt to excite the GaAs QDs via ARP.

The second topic presented is the build-up of a scanning FPI from scratch. After setting up the theoretical foundation of electromagnetic waves and different FPI setups, simulations were presented in order to determine component parameters suitable for the wanted FPI mode properties. Afterwards, measurements were presented, which involved aligning the FPI with a HeNe laser, mode matching and spatial filtering. Finally, measurements of the FSS of a GaAs QD were presented and evaluated in order to confirm the consistency between the measured and the simulated results for the free spectral range. The next steps will be to set up the FPI in the confocal mode and measure with it the FSS as well. It might be advisable to buy multiple sets of mirrors in order to fulfil different needs regarding spectral width and resolution. When this is accomplished the scanning FPI can be used as "black box", which comes into action whenever fine details of QD emission need to be resolved.

Don't refer all the time to the main text. Imagine I'm a reader from a different field. I read the abstract, the introduction and the summary/outlook. Now I should know what you did and why and what are the future plans. At this point I have no idea what MOSAIC is, I have no idea what a pulse expander is, etc. unless you give me a hint in the summary.



# **Appendix**



# Appendix A.

## Acronyms

<b>QKD</b>	quantum key distribution	
<b>BSM</b>	Bell state measurement .....	2
<b>QD</b>	quantum dot .....	2
<b>FSS</b>	fine structure splitting .....	2
<b>MBE</b>	molecular beam epitaxy .....	3
<b>CB</b>	conduction band.....	3
<b>VB</b>	valence band .....	3
<b>X</b>	exciton .....	4
<b>XX</b>	biexciton .....	4
<b>ZPL</b>	zero phonon line .....	8
<b>PSB</b>	phonon side band .....	8
<b>FCP</b>	Franc-Condon principles .....	8
<b>APD</b>	avalanche photodiode .....	13
<b>HBT</b>	Hanbury-Brown-Twiss .....	13
<b>BS</b>	beam splitter .....	13
<b>FWHM</b>	full width at half maximum .....	16
<b>MPL</b>	micro photo-luminescence .....	16
<b>ARP</b>	adiabatic rapid passage.....	19
<b>IAC</b>	interferometric autocorrelation .....	22
<b>MOSAIC</b>	modified-spectrum autointerferometric correlation .....	23
<b>FPI</b>	Fabry Pérot interferometer .....	31
<b>CCD</b>	charge-coupled device.....	50

## Appendix A. Acronyms

---

<b>NIM</b>	nuclear instrumentation module.....	50
<b>BNC</b>	Bayonet Neill-Concelman .....	50

# Bibliography

- [1] Igor Aharonovich, Dirk Englund, and Milos Toth. "Solid-state single-photon emitters." In: *Nature Photonics* 10.10 (Oct. 2016), pp. 631–641. ISSN: 1749-4885, 1749-4893. DOI: 10.1038/nphoton.2016.186. URL: <http://www.nature.com/articles/nphoton.2016.186> (visited on 07/29/2019) (cit. on p. 1).
- [2] Jonathan P. Dowling and Gerard J. Milburn. "Quantum technology: the second quantum revolution." In: *Philosophical Transactions of the Royal Society of London. Series A: Mathematical, Physical and Engineering Sciences* 361.1809 (Aug. 15, 2003). Ed. by A. G. J. MacFarlane, pp. 1655–1674. ISSN: 1471-2962. DOI: 10.1098/rsta.2003.1227. URL: <http://www.royalsocietypublishing.org/doi/10.1098/rsta.2003.1227> (visited on 07/08/2019) (cit. on p. 1).
- [3] Anton Zeilinger. "Light for the quantum. Entangled photons and their applications: a very personal perspective." In: *Physica Scripta* 92.7 (July 1, 2017), p. 072501. ISSN: 0031-8949, 1402-4896. DOI: 10.1088/1402-4896/aa736d. URL: <http://stacks.iop.org/1402-4896/92/i=7/a=072501?key=crossref.0e8a32b86987e059b0432176f8f5b174> (visited on 07/26/2019) (cit. on p. 1).
- [4] Nicolas Gisin et al. "Quantum cryptography." In: *Reviews of Modern Physics* 74.1 (Mar. 8, 2002), pp. 145–195. ISSN: 0034-6861, 1539-0756. DOI: 10.1103/RevModPhys.74.145. URL: <https://link.aps.org/doi/10.1103/RevModPhys.74.145> (visited on 07/26/2019) (cit. on p. 1).
- [5] Artur K. Ekert. "Quantum cryptography based on Bell's theorem." In: *Physical Review Letters* 67.6 (Aug. 5, 1991), pp. 661–663. ISSN: 0031-9007. DOI: 10.1103/PhysRevLett.67.661. URL: <https://link.aps.org/doi/10.1103/PhysRevLett.67.661> (visited on 07/18/2019) (cit. on p. 1).
- [6] Marcus Reindl et al. "All-photonic quantum teleportation using on-demand solid-state quantum emitters." In: *Science Advances* 4.12 (Dec. 2018), eaau1255. ISSN: 2375-2548. DOI: 10.1126/sciadv.aau1255. URL: <http://advances.sciencemag.org/lookup/doi/10.1126/sciadv.aau1255> (visited on 07/23/2019) (cit. on p. 1).

## Bibliography

---

- [7] L.-M. Duan et al. "Long-distance quantum communication with atomic ensembles and linear optics." In: *Nature* 414.6862 (Nov. 2001), pp. 413–418. ISSN: 0028-0836, 1476-4687. DOI: 10.1038/35106500. URL: <http://www.nature.com/articles/35106500> (visited on 07/26/2019) (cit. on p. 1).
- [8] Christoph Simon et al. "Quantum Repeaters with Photon Pair Sources and Multimode Memories." In: *Physical Review Letters* 98.19 (May 11, 2007). ISSN: 0031-9007, 1079-7114. DOI: 10.1103/PhysRevLett.98.190503. URL: <https://link.aps.org/doi/10.1103/PhysRevLett.98.190503> (visited on 07/26/2019) (cit. on p. 1).
- [9] Charles H. Bennett et al. "Teleporting an unknown quantum state via dual classical and Einstein-Podolsky-Rosen channels." In: *Physical Review Letters* 70.13 (Mar. 29, 1993), pp. 1895–1899. ISSN: 0031-9007. DOI: 10.1103/PhysRevLett.70.1895. URL: <https://link.aps.org/doi/10.1103/PhysRevLett.70.1895> (visited on 07/26/2019) (cit. on p. 2).
- [10] James L. Park. "The concept of transition in quantum mechanics." In: *Foundations of Physics* 1.1 (1970), pp. 23–33. ISSN: 0015-9018, 1572-9516. DOI: 10.1007/BF00708652. URL: <http://link.springer.com/10.1007/BF00708652> (visited on 07/29/2019) (cit. on p. 2).
- [11] Y. H. Shih and C. O. Alley. "New Type of Einstein-Podolsky-Rosen-Bohm Experiment Using Pairs of Light Quanta Produced by Optical Parametric Down Conversion." In: *Physical Review Letters* 61.26 (Dec. 26, 1988), pp. 2921–2924. ISSN: 0031-9007. DOI: 10.1103/PhysRevLett.61.2921. URL: <https://link.aps.org/doi/10.1103/PhysRevLett.61.2921> (visited on 07/26/2019) (cit. on p. 2).
- [12] Alain Aspect, Philippe Grangier, and Gérard Roger. "Experimental Tests of Realistic Local Theories via Bell's Theorem." In: *Physical Review Letters* 47.7 (Aug. 17, 1981), pp. 460–463. ISSN: 0031-9007. DOI: 10.1103/PhysRevLett.47.460. URL: <https://link.aps.org/doi/10.1103/PhysRevLett.47.460> (visited on 07/26/2019) (cit. on p. 2).
- [13] Axel Kuhn, Markus Hennrich, and Gerhard Rempe. "Deterministic Single-Photon Source for Distributed Quantum Networking." In: *Physical Review Letters* 89.6 (July 19, 2002). ISSN: 0031-9007, 1079-7114. DOI: 10.1103/PhysRevLett.89.067901. URL: <https://link.aps.org/doi/10.1103/PhysRevLett.89.067901> (visited on 07/26/2019) (cit. on p. 2).
- [14] Harishankar Jayakumar et al. "Deterministic Photon Pairs and Coherent Optical Control of a Single Quantum Dot." In: *Physical Review Letters* 110.13 (Mar. 26, 2013). ISSN: 0031-9007, 1079-7114. DOI: 10.1103/PhysRevLett.110.135505. URL: <https://link.aps.org/doi/10.1103/PhysRevLett.110.135505> (visited on 06/18/2019) (cit. on p. 2).

- [15] Daniel Huber. "GaAs quantum dots: A Dephasing-Free Source of Entangled Photon Pairs." PhD thesis. 2019 (cit. on pp. 3–5, 7, 11, 12).
- [16] Christian Schimpf. *Towards quantum teleportation with remote quantum dots*. 2017 (cit. on pp. 3, 7, 11–13, 15).
- [17] Zh. M. Wang et al. "Nanoholes fabricated by self-assembled gallium nanodrill on GaAs(100)." In: *Applied Physics Letters* 90.11 (Mar. 12, 2007), p. 113120. ISSN: 0003-6951, 1077-3118. DOI: 10.1063/1.2713745. URL: <http://aip.scitation.org/doi/10.1063/1.2713745> (visited on 06/13/2019) (cit. on p. 3).
- [18] Dieter Bimberg, Marius Grundmann, and Nikolai N. Ledentsov. *Quantum dot heterostructures*. Chichester, [Eng.]; New York: John Wiley, 1999. 328 pp. ISBN: 978-0-471-97388-1 (cit. on p. 4).
- [19] R. M. Stevenson et al. "A semiconductor source of triggered entangled photon pairs." In: *Nature* 439.7073 (Jan. 2006), pp. 179–182. ISSN: 0028-0836, 1476-4687. DOI: 10.1038/nature04446. URL: <http://www.nature.com/articles/nature04446> (visited on 06/17/2019) (cit. on p. 4).
- [20] M. Bayer et al. "Fine structure of neutral and charged excitons in self-assembled In(Ga)As/(Al)GaAs quantum dots." In: *Physical Review B* 65.19 (May 7, 2002). ISSN: 0163-1829, 1095-3795. DOI: 10.1103/PhysRevB.65.195315. URL: <https://link.aps.org/doi/10.1103/PhysRevB.65.195315> (visited on 06/17/2019) (cit. on p. 6).
- [21] E. Peter et al. "Phonon sidebands in exciton and biexciton emission from single GaAs quantum dots." In: *Physical Review B* 69.4 (Jan. 26, 2004), p. 041307. ISSN: 1098-0121, 1550-235X. DOI: 10.1103/PhysRevB.69.041307. URL: <https://link.aps.org/doi/10.1103/PhysRevB.69.041307> (visited on 06/11/2019) (cit. on p. 8).
- [22] Antoine Reigue et al. "Probing Electron-Phonon Interaction through Two-Photon Interference in Resonantly Driven Semiconductor Quantum Dots." In: *Physical Review Letters* 118.23 (June 6, 2017). ISSN: 0031-9007, 1079-7114. DOI: 10.1103/PhysRevLett.118.233602. URL: <http://link.aps.org/doi/10.1103/PhysRevLett.118.233602> (visited on 07/23/2019) (cit. on p. 8).
- [23] Josef Friedrich and Dietrich Haarer. "Photochemical Hole Burning: A Spectroscopic Study of Relaxation Processes in Polymers and Glasses." In: *Angewandte Chemie International Edition in English* 23.2 (Feb. 1984), pp. 113–140. ISSN: 0570-0833, 1521-3773. DOI: 10.1002/anie.198401131. URL: <http://doi.wiley.com/10.1002/anie.198401131> (visited on 06/11/2019) (cit. on p. 8).
- [24] J. Franck and E. G. Dymond. "Elementary processes of photochemical reactions." In: *Transactions of the Faraday Society* 21 (February 1926), p. 536. ISSN: 0014-7672. DOI: 10.1039/tf9262100536. URL: <http://xlink.rsc.org/?DOI=tf9262100536> (visited on 07/22/2019) (cit. on p. 8).

## Bibliography

---

- [25] *Zero-phonon line and phonon sideband - Wikipedia*. URL: [https://en.wikipedia.org/wiki/Zero-phonon\\_line\\_and\\_phonon\\_sideband](https://en.wikipedia.org/wiki/Zero-phonon_line_and_phonon_sideband) (visited on 06/11/2019) (cit. on p. 9).
- [26] Eva Schöll et al. "Resonance fluorescence of GaAs quantum dots with near-unity photon indistinguishability." In: *Nano Letters* 19.4 (Apr. 10, 2019), pp. 2404–2410. ISSN: 1530-6984, 1530-6992. DOI: 10.1021/acs.nanolett.8b05132. arXiv: 1901.09721. URL: <http://arxiv.org/abs/1901.09721> (visited on 05/09/2019) (cit. on p. 10).
- [27] Takashi Kuroda et al. "Symmetric quantum dots as efficient sources of highly entangled photons: Violation of Bell's inequality without spectral and temporal filtering." In: *Physical Review B* 88.4 (July 18, 2013). ISSN: 1098-0121, 1550-235X. DOI: 10.1103/PhysRevB.88.041306. URL: <https://link.aps.org/doi/10.1103/PhysRevB.88.041306> (visited on 06/18/2019) (cit. on p. 11).
- [28] Peter Michler, ed. *Single semiconductor quantum dots*. Nanoscience and technology. OCLC: ocn248993461. Berlin: Springer, 2009. 389 pp. ISBN: 978-3-540-87445-4 978-3-540-87446-1 (cit. on p. 11).
- [29] Marcus Reindl et al. "Phonon-Assisted Two-Photon Interference from Remote Quantum Emitters." In: *Nano Letters* 17.7 (July 12, 2017), pp. 4090–4095. ISSN: 1530-6984, 1530-6992. DOI: 10.1021/acs.nanolett.7b00777. URL: <http://pubs.acs.org/doi/10.1021/acs.nanolett.7b00777> (visited on 06/19/2019) (cit. on pp. 11, 12).
- [30] S. Stufler et al. "Two-photon Rabi oscillations in a single In<sub>x</sub>Ga<sub>1-x</sub>AsGaAs quantum dot." In: *Physical Review B* 73.12 (Mar. 7, 2006). ISSN: 1098-0121, 1550-235X. DOI: 10.1103/PhysRevB.73.125304. URL: <https://link.aps.org/doi/10.1103/PhysRevB.73.125304> (visited on 06/19/2019) (cit. on p. 12).
- [31] J. Förstner et al. "Phonon-Assisted Damping of Rabi Oscillations in Semiconductor Quantum Dots." In: *Physical Review Letters* 91.12 (Sept. 16, 2003). ISSN: 0031-9007, 1079-7114. DOI: 10.1103/PhysRevLett.91.127401. URL: <https://link.aps.org/doi/10.1103/PhysRevLett.91.127401> (visited on 06/19/2019) (cit. on p. 12).
- [32] Marcus Reindl. *Characterisation of semiconductor quantum dots by means of advanced optical spectroscopy techniques*. 2014 (cit. on pp. 16, 17).
- [33] M. Glässl et al. "Biexciton state preparation in a quantum dot via adiabatic rapid passage: Comparison between two control protocols and impact of phonon-induced dephasing." In: *Physical Review B* 87.8 (Feb. 8, 2013). ISSN: 1098-0121, 1550-235X. DOI: 10.1103/PhysRevB.87.085303. URL: <https://link.aps.org/doi/10.1103/PhysRevB.87.085303> (visited on 05/13/2019) (cit. on pp. 20, 26, 27).

- [34] Toshiyuki Hirayama and Mansoor Sheik-Bahae. "Real-time chirp diagnostic for ultrashort laser pulses." In: *Optics Letters* 27.10 (May 15, 2002), p. 860. ISSN: 0146-9592, 1539-4794. DOI: 10.1364/OL.27.000860. URL: <https://www.osapublishing.org/abstract.cfm?URI=ol-27-10-860> (visited on 05/13/2019) (cit. on pp. 20, 23).
- [35] Optical autocorrelation - Wikipedia. URL: [https://en.wikipedia.org/wiki/Optical\\_autocorrelation](https://en.wikipedia.org/wiki/Optical_autocorrelation) (visited on 06/25/2019) (cit. on p. 22).
- [36] Jean-Claude Diels and Wolfgang Rudolph. *Ultrashort laser pulse phenomena: fundamentals, techniques, and applications on a femtosecond time scale*. 2nd ed. Optics and photonics. Amsterdam ; Boston: Elsevier / Academic Press, 2006. 652 pp. ISBN: 978-0-12-215493-5 (cit. on p. 22).
- [37] Miles V. Klein and Thomas E. Furtak. *Optics*. 2nd ed. New York: Wiley, 1986. 660 pp. ISBN: 978-0-471-87297-9 (cit. on p. 24).
- [38] O. Martinez. "3000 times grating compressor with positive group velocity dispersion: Application to fiber compensation in 1.3–1.6 um region." In: *IEEE Journal of Quantum Electronics* 23.1 (Jan. 1987), pp. 59–64. ISSN: 0018-9197. DOI: 10.1109/JQE.1987.1073201. URL: <http://ieeexplore.ieee.org/document/1073201/> (visited on 06/28/2019) (cit. on pp. 25, 26).
- [39] Sophocles J. Orfanidis. *Electromagnetic waves and antennas*. 2002 (cit. on p. 26).
- [40] V.S. Malinovsky and J.L. Krause. "General theory of population transfer by adiabatic rapid passage with intense, chirped laser pulses." In: *The European Physical Journal D* 14.2 (May 2001), pp. 147–155. ISSN: 14346060. DOI: 10.1007/s100530170212. URL: <http://www.springerlink.com/index/10.1007/s100530170212> (visited on 07/22/2019) (cit. on p. 27).
- [41] Timo Kaldewey et al. "Coherent and robust high-fidelity generation of a biexciton in a quantum dot by rapid adiabatic passage." In: *Physical Review B* 95.16 (Apr. 10, 2017). ISSN: 2469-9950, 2469-9969. DOI: 10.1103/PhysRevB.95.161302. arXiv: 1701.01371. URL: <http://arxiv.org/abs/1701.01371> (visited on 12/11/2018) (cit. on p. 31).
- [42] Dieter Meschede. *Optik, Licht und Laser*. 3., durchges. Aufl. Studium. OCLC: 254422596. Wiesbaden: Vieweg + Teubner, 2008. 568 pp. ISBN: 978-3-8351-0143-2 (cit. on pp. 31, 33, 40, 43).
- [43] Nur Ismail et al. "Fabry-Pérot resonator: spectral line shapes, generic and related Airy distributions, linewidths, finesse, and performance at low or frequency-dependent reflectivity." In: *Optics Express* 24.15 (July 25, 2016), p. 16366. ISSN: 1094-4087. DOI: 10.1364/OE.24.016366. URL: <https://www.osapublishing.org/abstract.cfm?URI=oe-24-15-16366> (visited on 05/13/2019) (cit. on pp. 35, 37).

## Bibliography

---

- [44] *Fabry–Pérot interferometer - Wikipedia*. URL: [https://en.wikipedia.org/wiki/Fabry%25E2%2580%2593P%C3%A9rot\\_interferometer](https://en.wikipedia.org/wiki/Fabry%25E2%2580%2593P%C3%A9rot_interferometer) (visited on 05/06/2019) (cit. on pp. 37–39).
- [45] Amnon Yariv, Pochi Yeh, and Amnon Yariv. *Photonics: optical electronics in modern communications*. 6th ed. The Oxford series in electrical and computer engineering. OCLC: ocm58648003. New York: Oxford University Press, 2007. 836 pp. ISBN: 978-0-19-517946-0 (cit. on p. 40).
- [46] Michael Hercher. “The Spherical Mirror Fabry-Perot Interferometer.” In: *Applied Optics* 7.5 (May 1, 1968), p. 951. ISSN: 0003-6935, 1539-4522. DOI: 10.1364/AO.7.000951. URL: <https://www.osapublishing.org/abstract.cfm?URI=ao-7-5-951> (visited on 05/09/2019) (cit. on p. 43).